Article

Moving-Target Detection for FDA-MIMO Radar in Partially Homogeneous Environments

Changshan He [1,2], Running Zhang [2], Bang Huang [3], Mingming Xu [2], Zhibin Wang [2], Lei Liu [2], Zheng Lu [2] and Ye Jin [1,4,*]

1   School of Information and Electronics, Beijing Institute of Technology, Beijing 100081, China; thechangshan@spacechina.com
2   Institute of Remote Sensing Satellite, China Academy of Space Technology, Beijing 100094, China; zhangrunningdfh@spacechina.com (R.Z.); xumingming@spacechina.com (M.X.); wangzhibin1@spacechina.com (Z.W.); liulei4@spacechina.com (L.L.); lvzheng_irss@spacechina.com (Z.L.)
3   School of Information and Communication Engineering, University of Electronic Science and Technology of China, Chengdu 611731, China; huangbang@std.uestc.edu.cn
4   Key Laboratory of Electronics and Information Technology in Satellite Navigation (Beijing Institute of Technology), Ministry of Education, Beijing 100081, China
*   Correspondence: bitjinye@bit.edu.cn

Abstract: This paper delves into the problem of moving-target detection in partially homogeneous environments (PHE) with unknown Gaussian disturbance using a frequency diverse array multiple-input multiple-output (FDA-MIMO) radar. Using training data, we have derived expressions for four adaptive detectors, including the one-step and two-step generalized likelihood ratio test (GLRT), two-step Rao (TRao) test, and two-step Wald (TWald) test criteria, respectively. All the proposed detectors are characterized by the constant false-alarm rate (CFAR). The theoretical analysis and simulation results validate the effectiveness of the proposed detectors.

Keywords: FDA-MIMO radar; partially homogeneous environments; moving-target detection; OGLRT; TGLRT; TRao test; TWald test

1. Introduction

The frequency diverse array (FDA) was first introduced by Antonik at the 2006 IEEE Radar Conference [1]. Since then, it has gained significant attention from the radar community [2–6] due to its various advantages over traditional phased arrays (PAs). The FDA radar uses a small frequency increment across its array elements to produce a range-angle-time dependent beampattern. This range and time dependency allows for more degrees of freedom (DOFs) in operating the beampattern for improved performance. However, the time dependency and range-angle coupled beampattern can sometimes pose challenges for accurate target detection and estimation. To address these issues, a frequency diverse array multiple-input multiple-output (FDA-MIMO) radar has been developed by combining an FDA with a MIMO system, which is presented in the literature [7]. This innovative technology effectively eliminates time-variance and coupling effects while preserving target information [8–10]. The FDA-MIMO radar has a wide range of applications, including secure physical layer communications [11], high-resolution and wide-swath synthetic aperture radar (HRWS-SAR) imaging [12,13], SAR deceptive jamming rejection [14–16], and more. By discriminating echoes at different distances, the mainlobe interferences [17], mainlobe clutter [18], main-beam deceptive jamming [9,10,17,19–21], etc., can be effectively suppressed using the FDA-MIMO-based range information.

Accurate target detection is a critical aspect of radar performance, and FDA-MIMO radars are no different. However, target detection in diverse environments using FDA-MIMO radars [18,22–24] has yet to be thoroughly investigated. For instance, Gui et al. [23] developed a low complexity unstructured generalized likelihood ratio test (UGLRT) approach for an

FDA-MIMO radar in the case of an unknown interference covariance matrix (ICM), including deceptive and suppressive jamming. Huang et al. [25] investigated the target detection problem in an interference background using the Rao and Wald principles. Please note that these approaches did not use any training data to estimate the interference covariance due to the range dependency of the deceptive jamming covariance matrix for an FDA-MIMO radar. Therefore, the covariance matrix of the training data sampled from near-range cells does not apply to the current cell under test (CUT). However, techniques such as secondary range dependence compensation [26] can help overcome the range dependency and acquire independent and identically distributed (IID) training data, which allows the estimation of the unknown covariance matrix and improves detection performance. Therefore, Lan et al. [22] analyzed the FDA-MIMO-based target detection problem with training data in the case of an unknown interference-plus-noise covariance matrix according to the traditional generalized likelihood ratio test (GLRT) criterion. Chen et al. [27] proposed a space-range-doppler focus-based moving-target detection approach that utilized training data for an FDA-MIMO radar in clutter and noise environments. Li et al. [28] adopted the GLRT criterion and used training data to design adaptive detectors for an FDA-MIMO radar in the cases of known and unknown target velocity with unknown Gaussian noise. Please note that the training and test data observe a common covariance matrix in the aforementioned detectors, i.e., homogeneous environments (HE). Nevertheless, in practice, it is rare to find completely homogeneous environments due to various environmental and instrumental factors. When the terrain is undulating, there may be power variations between the training and test data. This leads to partially homogeneous environments, which is a commonly held assumption when dealing with nonhomogeneous environments. In partially homogeneous environments, it is assumed that the training and test data observe the same covariance matrix up to an unknown scaling factor [29–31], which helps to improve the robustness against noise power level variations between the training and test data [32]. If the scaling factor equals 1, then the radar operates in a homogeneous environment; otherwise, it operates in a partially homogeneous environment. The partial homogeneity assumption is critical for airborne and ground-based radars [30,33] as it provides an accurate scenario description. Consequently, it is necessary to thoroughly investigate target detection methods in partially homogeneous environments for an FDA-MIMO radar.

In this paper, we thoroughly investigate adaptive detectors with training data for an FDA-MIMO radar in partially homogeneous Gaussian disturbance environments where thermal noise, mainlobe deceptive jamming, and range-compensated clutter exist. It should be noted that finding a uniformly optimal detector for this detection problem is nearly impossible, but we can still explore suboptimal detectors. As common detector design guidelines, it has been found that the one-step GLRT (OGLRT) offers superior detection performance [30], while the two-step GLRT (TGLRT) performs similarly to OGLRT but with less computation. Additionally, the two-step Rao (TRao) test and two-step Wald (TWald) test exhibit greater selectivity or robustness to signal mismatch while also reducing computational complexity [34,35]. Therefore, these four criteria will be utilized to design adaptive detectors for the FDA-MIMO radar-based target detection problem. We evaluate the detection performance in partially homogeneous environments and prove that the detectors demonstrate a constant false-alarm rate (CFAR) property against the covariance matrix and the scaling factor. The experimental outcomes demonstrate that the proposed OGLRT detector outperforms the other proposed detectors when steering vectors match. In contrast, the other proposed detectors exhibit superior detection performance when steering vectors mismatch. The main contributions of this paper are summarized as follows:

(1) This study is the first to explore the target detection problem for an FDA-MIMO radar in partially homogeneous environments and illustrates that the proposed methods are general since they can also be applied in homogeneous environments.

(2) With training data, four adaptive detectors are designed for FDA-MIMO radar based on the OGLRT, TGLRT, TRao, and TWald methods, and it is proven that they have a CFAR property for the covariance matrix and the scaling factor.

The remaining sections of this paper are structured as follows: the next section introduces the problem of moving-target detection for FDA-MIMO radar. Section 3 derives the detectors with training data. Section 4 investigates the CFAR property of the proposed detectors. Section 5 assesses the performance of proposed detectors by Monte Carlo (MC) simulations. Section 6 draws conclusions.

2. Problem Formulation

Consider an FDA-MIMO radar with an M-element FDA transmitter and an N-element PA receiver for a far-field scenario. The inter-element spacings of transmit and receive arrays are set to be d_T and d_R, respectively. Suppose a point-like moving target is located at (r_s, θ_s), where r_s is the slant range and θ_s represents the azimuth angle. The target is moving at a constant radial velocity v towards the radar. After mixed and matched filtered, the kth snapshot of an FDA-MIMO signal (using frequency-shifted orthogonal waveforms with large frequency increments leads the waveform correlation matrix to an identity matrix [23]) can be mathematically modeled as [36]

$$\mathbf{x}_k = \alpha_s \omega_k(f_{d,s}) \mathbf{a}_{tr}(r_s, \theta_s) + \mathbf{n}_k, \tag{1}$$

where α_s is the unknown complex amplitude depending on both the radar cross section (RCS) and the propagation coefficient. The moving-target Doppler has the form $\omega_k(f_{d,s}) = e^{j2\pi f_{d,s} k} / \sqrt{K}$, with K and $f_{d,s} = 2v f_0 T_{PR} / c$ being the total number of transmit pulses and the relative Doppler frequency caused by the moving-target, respectively. Additionally, c, f_0, and T_{PR} represent the speed of light, reference carrier frequency, and pulse repetition interval (PRI), respectively. Moreover, $\mathbf{a}_{tr}(r_s, \theta_s)$ is the joint transmit-receive steering vector, defined as

$$\mathbf{a}_{tr}(r_s, \theta_s) \triangleq \mathbf{a}_t(r_s, \theta_s) \otimes \mathbf{a}_r(\theta_s) \in \mathbb{C}^{MN \times 1}, \tag{2}$$

where $\otimes$ is the Kronecker product, and $\mathbf{a}_t(r_s, \theta_s)$ stands for the transmit steering vector, given by

$$\mathbf{a}_t(r_s, \theta_s) \triangleq \mathbf{a}_t(\theta_s) \odot \mathbf{e}(-\tau) \in \mathbb{C}^{M \times 1}, \tag{3}$$

where $\odot$ is the Hadamard product, with

$$\mathbf{a}_t(\theta_s) = \left[1, e^{j2\pi \frac{d_T}{\lambda_0} \sin \theta_s}, \cdots, e^{j2\pi \frac{d_T}{\lambda_0} (M-1) \sin \theta_s} \right]^T \in \mathbb{C}^{M \times 1}, \tag{4}$$

and

$$\mathbf{e}(t) = \left[1, e^{j2\pi \Delta f t}, \cdots, e^{j2\pi (M-1) \Delta f t} \right]^T \in \mathbb{C}^{M \times 1}, \tag{5}$$

representing the transmit array vector and the carrier vector, respectively. The notation $(\cdot)^T$ stands for the matrix (vector) transpose, λ_0 is the wavelength corresponding to f_0, Δf stands for the inter-element frequency increment in the transmit array, and $\tau = 2r_s / c$ is the two-way time delay. The receive steering vector $\mathbf{a}_r(\theta_s)$ is given by,

$$\mathbf{a}_r(\theta_s) = \left[1, e^{j2\pi \frac{d_R}{\lambda_0} \sin \theta_s}, \cdots, e^{j2\pi \frac{d_R}{\lambda_0} (N-1) \sin \theta_s} \right]^T \in \mathbb{C}^{N \times 1}, \tag{6}$$

Finally, the additive term $\mathbf{n}_k \in \mathbb{C}^{MN \times 1}$ represents the Gaussian noise (thermal noise, mainlobe deceptive jamming and range-compensated clutter) in the receiver array.

Furthermore, jointly processing over K snapshots (For the sake of mathematical convenience, assume that the target motion does not cross the range cell or undergo a Doppler shift during the K snapshots.), we can obtain the received data in a matrix form, expressed as [23]:

$$\mathbf{X} = \alpha_s \mathbf{a}_{tr}(r_s, \theta_s) \mathbf{w}_d^T(f_{d,s}) + \mathbf{N} \in \mathbb{C}^{MN \times K}, \tag{7}$$

where

$$\mathbf{X} = [\mathbf{x}_0, \mathbf{x}_1, \cdots, \mathbf{x}_{K-1}] \in \mathbb{C}^{MN \times K}, \tag{8}$$

$$\mathbf{w}_d(f_{d,s}) = [\omega_0(f_{d,s}), \omega_1(f_{d,s}), \cdots, \omega_{K-1}(f_{d,s})]^T \in \mathbb{C}^{K \times 1}, \tag{9}$$

and

$$\mathbf{N} = [\mathbf{n}_0, \mathbf{n}_1, \cdots, \mathbf{n}_{K-1}] \in \mathbb{C}^{MN \times K}. \tag{10}$$

In addition, a set of available training data $\mathbf{X}_l = \mathbf{N}_l \in \mathbb{C}^{MN \times K}, l = 1, 2, \cdots, L$, is sampled from the neighboring range cells, which only contain noise, with $\mathbf{n}_{l,k}^s \in \mathbb{C}^{MN \times 1}$ representing the kth column of lth training data matrix $\mathbf{N}_l$. The noise terms $\mathbf{n}_k$ and $\mathbf{n}_{l,k}^s$, $k = 0, 1, \cdots, K-1$, are modeled as zero-mean circularly complex Gaussian independent random vectors with unknown positive definite covariance matrices $\mathbf{R}_t$ and $\mathbf{R}$, i.e., $\mathbf{n}_k \sim \mathrm{CN}(0, \mathbf{R}_t)$ and $\mathbf{n}_{l,k}^s \sim \mathrm{CN}(0, \mathbf{R})$, respectively. The assumption of a partially homogeneous environment implies that the covariance matrix of the training data is related to that of the test data with a constant scaling factor, so we have:

$$\mathbf{R}_t = \gamma \mathbf{R}, \tag{11}$$

where γ is a positive value representing the power mismatch between the two matrices. In particular, when $\gamma = 1$, the covariance matrices are identical, indicating that the current detection environments are under the homogeneity assumption.

Hence, the FDA-MIMO radar-based detection problem can be formulated as a binary hypotheses test:

$$\begin{cases} H_0 : \begin{cases} \mathbf{X} = \mathbf{N}, \\ \mathbf{X}_l = \mathbf{N}_l, l = 1, 2, \cdots, L, \end{cases} \\ H_1 : \begin{cases} \mathbf{X} = \alpha_s \mathbf{a}_{tr}(r_s, \theta_s) \mathbf{w}_d^T(f_{d,s}) + \mathbf{N}, \\ \mathbf{X}_l = \mathbf{N}_l, l = 1, 2, \cdots, L. \end{cases} \end{cases} \tag{12}$$

where the null hypothesis H_0 represents target absence, whereas the alternative hypothesis H_1 indicates target presence. Please note that in (12), $\mathbf{a}_{tr}(r_s, \theta_s)$ and $\mathbf{w}_d(f_{d,s})$ are both known, while α_s, γ and $\mathbf{R}$ remain unknown. It is important to point out that this paper takes a different approach compared to the literature [28], as we address the target detection problem for the FDA-MIMO radar in partially homogeneous environments, whereas the literature [28] concentrated solely on designing OGLRT-based detectors in homogeneous environments. Additionally, we will demonstrate that our proposed detectors are effective in solving the detection problem for the FDA-MIMO radar in both homogeneous and partially homogeneous environments. Subsequently, for notational brevity, we replace $\mathbf{a}_{tr}(r_s, \theta_s)$ and $\mathbf{w}_d(f_{d,s})$ with $\mathbf{a}_{tr}$ and $\mathbf{w}_d$, respectively.

For future reference, we define $\mathbf{Y} = [\mathbf{X}_1, \mathbf{X}_2, \cdots, \mathbf{X}_L] \in \mathbb{C}^{MN \times LK}$, then the joint probability density function (PDF) of $\mathbf{X}$ and $\mathbf{Y}$ under hypothesis H_0 is

$$f(\mathbf{X}, \mathbf{Y}|\gamma, \mathbf{R}, H_0) = \frac{e^{-\mathrm{tr}(\mathbf{R}^{-1}\mathbf{X}\mathbf{X}^H/\gamma)} e^{-\mathrm{tr}(\mathbf{R}^{-1}\mathbf{S})}}{\pi^{MNK(L+1)} \gamma^{MNK} \det^{K(L+1)}(\mathbf{R})} \tag{13}$$

where $\mathbf{S} = \mathbf{Y}\mathbf{Y}^H \in \mathbb{C}^{MN \times MN}$ is KL times sample covariance matrix (SCM). Please note that to obtain a nonsingular covariance matrix estimate, it is necessary to ensure $KL \geq MN$. The symbols $tr(\cdot)$ and $\det(\cdot)$ represent the trace and the determinant of a matrix, respectively. Meanwhile, the notations $(\cdot)^H$ and $(\cdot)^{-1}$ denote the conjugate transpose and inverse of the nonsingular matrix argument, respectively.

Similarly, the joint PDF of $\mathbf{X}$ and $\mathbf{Y}$ under hypothesis H_1 is

$$f(\mathbf{X}, \mathbf{Y}|\alpha_s, \gamma, \mathbf{R}, H_1) = \frac{e^{-\mathrm{tr}(\mathbf{R}^{-1}\mathbf{X}_{\alpha_s}\mathbf{X}_{\alpha_s}^H/\gamma)} e^{-\mathrm{tr}(\mathbf{R}^{-1}\mathbf{S})}}{\pi^{MNK(L+1)} \gamma^{MNK} \det^{K(L+1)}(\mathbf{R})} \tag{14}$$

where $\mathbf{X}_{\alpha_s} = \mathbf{X} - \alpha_s \mathbf{a}_{tr} \mathbf{w}_d^T \in \mathbb{C}^{MN \times K}$.

3. Detector Design

In this section, we use the training data and apply the OGLRT, TGLRT, TRao test, and TWald test to design detectors for an FDA-MIMO radar.

3.1. OGLRT

According to the OGLRT criterion, the decision statistics are given by [37]

$$\Lambda_{OGLRT-PHE} = \frac{\max\limits_{\alpha_s, \gamma, \mathbf{R}} f(\mathbf{X}, \mathbf{Y} | \alpha_s, \gamma, \mathbf{R}, H_1)}{\max\limits_{\gamma, \mathbf{R}} f(\mathbf{X}, \mathbf{Y} | \gamma, \mathbf{R}, H_0)} \underset{H_0}{\overset{H_1}{\gtrless}} \lambda_{OGLRT-PHE}, \tag{15}$$

where $\lambda_{OGLRT-PHE}$ is the detection threshold.

To derive OGLRT, we need to maximize both the numerator and denominator of (15), respectively. We accomplish this by taking the logarithm of (14) and then taking its derivative with respect to $\mathbf{R}$, resulting in

$$\frac{\partial}{\partial \mathbf{R}} \ln f(\mathbf{X}, \mathbf{Y} | \alpha_s, \gamma, \mathbf{R}, H_1) = \mathbf{R}^{-1} \left(\frac{\mathbf{X}_{\alpha_s} \mathbf{X}_{\alpha_s}^H}{\gamma} + \mathbf{S} \right) \mathbf{R}^{-1} - K(L+1) \mathbf{R}^{-1}, \tag{16}$$

where the symbols $\partial(\cdot)$ and $\ln(\cdot)$ denote partial derivative and natural logarithm, respectively. Equation (16) to zero gives the maximum likelihood estimate (MLE) of $\mathbf{R}$ under hypothesis H_1 as

$$\hat{\mathbf{R}}_1 = \frac{1}{K(L+1)} \left(\frac{\mathbf{X}_{\alpha_s} \mathbf{X}_{\alpha_s}^H}{\gamma} + \mathbf{S} \right). \tag{17}$$

Plugging above expression into (14) and applying $\det(\mathbf{I} + \mathbf{AB}) = \det(\mathbf{I} + \mathbf{BA})$ for any applicable matrices, lead to

$$\begin{aligned} f(\mathbf{X}, \mathbf{Y} | \alpha_s, \gamma, \hat{\mathbf{R}}_1, H_1) &= \frac{\beta \det^{-K(L+1)}(\mathbf{S})}{\gamma^{MNK} \det^{K(L+1)} \left(\mathbf{I}_K + \mathbf{X}_{\alpha_s}^H \mathbf{S}^{-1} \mathbf{X}_{\alpha_s} / \gamma \right)} \\ &= \frac{\beta \det^{-K(L+1)}(\mathbf{S})}{\gamma^{MNK} \det^{K(L+1)} \left(\mathbf{I}_K + \tilde{\mathbf{X}}_{\alpha_s}^H \tilde{\mathbf{X}}_{\alpha_s} / \gamma \right)}, \end{aligned} \tag{18}$$

where $\beta = [K(L+1)/e\pi]^{MNK(L+1)}$, $\tilde{\mathbf{X}}_{\alpha_s} = \mathbf{S}^{-1/2} \mathbf{X}_{\alpha_s} = \tilde{\mathbf{X}} - \alpha_s \tilde{\mathbf{a}} \mathbf{w}_d^T$ with $\tilde{\mathbf{X}} = \mathbf{S}^{-1/2} \mathbf{X}$ and $\tilde{\mathbf{a}} = \mathbf{S}^{-1/2} \mathbf{a}_{tr}$, and $\mathbf{I}_K$ denotes the identity matrix of $K \times K$. It is apparent that maximizing (18) over α_s is tantamount to minimizing (19), as following

$$f(\alpha_s) = \det \left(\mathbf{I}_K + \frac{\tilde{\mathbf{X}}_{\alpha_s}^H \tilde{\mathbf{X}}_{\alpha_s}}{\gamma} \right). \tag{19}$$

In accordance with the theorem presented in [38], we can obtain the MLE of α_s and the minimum of $f(\alpha_s)$ as

$$\hat{\alpha}_s = \frac{\tilde{\mathbf{a}}^H \tilde{\mathbf{X}} \mathbf{w}_d^*}{\tilde{\mathbf{a}}^H \tilde{\mathbf{a}}}, \tag{20}$$

and

$$f(\hat{\alpha}_s) = \det \left[\mathbf{I}_k + \frac{\left(\tilde{\mathbf{X}} - \mathbf{P}_{\tilde{\mathbf{a}}} \tilde{\mathbf{X}} \mathbf{w}_d^* \mathbf{w}_d^T \right)^H \left(\tilde{\mathbf{X}} - \mathbf{P}_{\tilde{\mathbf{a}}} \tilde{\mathbf{X}} \mathbf{w}_d^* \mathbf{w}_d^T \right)}{\gamma} \right], \tag{21}$$

respectively, where $\mathbf{P}_{\tilde{\mathbf{a}}} = \frac{\tilde{\mathbf{a}}\tilde{\mathbf{a}}^H}{\tilde{\mathbf{a}}^H\tilde{\mathbf{a}}}$ is the projection matrix onto the column space of $\tilde{\mathbf{a}}$. Appendix A provides a detailed derivation of these results. Substituting (21) into (18) yields

$$f\left(\mathbf{X}, \mathbf{Y}|\hat{\alpha}_s, \gamma, \hat{\mathbf{R}}_1, H_1\right) = \frac{\beta \det^{-K(L+1)}(\mathbf{S})}{\gamma^{MNK} \det^{K(L+1)}\left[\mathbf{I}_K + \frac{\left(\tilde{\mathbf{X}} - \mathbf{P}_{\tilde{\mathbf{a}}}\tilde{\mathbf{X}}\mathbf{w}_d^*\mathbf{w}_d^T\right)^H\left(\tilde{\mathbf{X}} - \mathbf{P}_{\tilde{\mathbf{a}}}\tilde{\mathbf{X}}\mathbf{w}_d^*\mathbf{w}_d^T\right)}{\gamma}\right]}. \tag{22}$$

Likewise (17), we also have the MLE of $\mathbf{R}$ under hypothesis H_0 as

$$\hat{\mathbf{R}}_0 = \frac{1}{K(L+1)}\left(\frac{\mathbf{X}\mathbf{X}^H}{\gamma} + \mathbf{S}\right). \tag{23}$$

Substituting (23) into (13) leads to

$$f\left(\mathbf{X}, \mathbf{Y}|\gamma, \hat{\mathbf{R}}_0, H_0\right) = \frac{\beta \det^{-K(L+1)}(\mathbf{S})}{\gamma^{MNK} \det^{K(L+1)}\left(\mathbf{I}_K + \frac{\tilde{\mathbf{X}}^H\tilde{\mathbf{X}}}{\gamma}\right)}, \tag{24}$$

where the determinant lemma is used once again. We can then insert (22) and (24) into (15) and take its $K(L+1)$th root to obtain

$$\Lambda'_{OGLRT-PHE} = \frac{\min\limits_{\gamma} \gamma^{\frac{MN}{L+1}} \det\left[\mathbf{I}_K + \frac{\tilde{\mathbf{X}}^H\tilde{\mathbf{X}}}{\gamma}\right]}{\min\limits_{\gamma} \gamma^{\frac{MN}{L+1}} \det\left[\mathbf{I}_K + \frac{\left(\tilde{\mathbf{X}} - \mathbf{P}_{\tilde{\mathbf{a}}}\tilde{\mathbf{X}}\mathbf{w}_d^*\mathbf{w}_d^T\right)^H\left(\tilde{\mathbf{X}} - \mathbf{P}_{\tilde{\mathbf{a}}}\tilde{\mathbf{X}}\mathbf{w}_d^*\mathbf{w}_d^T\right)}{\gamma}\right]} \underset{H_0}{\overset{H_1}{\gtrless}} \lambda'_{OGLRT-PHE}, \tag{25}$$

where $\lambda'_{OGLRT-PHE}$ denotes a modification of the threshold in (15).

Assuming that $\hat{\gamma}_0$ and $\hat{\gamma}_1$ are the MLEs of γ under hypotheses H_0 and H_1 respectively. The technique used in [39] is adopted to find the solution for $\hat{\gamma}_i (i = 0, 1)$, which is the unique positive solution to the following equation

$$\sum_{r=1}^{R} \frac{\delta_{r,i}}{\delta_{r,i} + x} = \frac{MN}{L+1}, \tag{26}$$

where $R = \min(MN, K)$, x denotes the unknown, $\delta_{r,0}$ and $\delta_{r,1}$ represent the rth non-zero eigenvalues of the matrices $\tilde{\mathbf{X}}^H\tilde{\mathbf{X}}$ and $\left(\tilde{\mathbf{X}} - \mathbf{P}_{\tilde{\mathbf{a}}}\tilde{\mathbf{X}}\mathbf{w}_d^*\mathbf{w}_d^T\right)^H\left(\tilde{\mathbf{X}} - \mathbf{P}_{\tilde{\mathbf{a}}}\tilde{\mathbf{X}}\mathbf{w}_d^*\mathbf{w}_d^T\right)$, respectively. The detailed derivations of the above results are provided in Appendix B. Once we have found $\hat{\gamma}_i (i = 0, 1)$, it is inserted into (25), and we obtain the final OGLRT detector as

$$\Lambda'_{OGLRT-PHE} = \frac{\hat{\gamma}_0^{\frac{MN}{L+1}} \det\left[\mathbf{I}_K + \frac{\tilde{\mathbf{X}}^H\tilde{\mathbf{X}}}{\hat{\gamma}_0}\right]}{\hat{\gamma}_1^{\frac{MN}{L+1}} \det\left[\mathbf{I}_K + \frac{\left(\tilde{\mathbf{X}} - \mathbf{P}_{\tilde{\mathbf{a}}}\tilde{\mathbf{X}}\mathbf{w}_d^*\mathbf{w}_d^T\right)^H\left(\tilde{\mathbf{X}} - \mathbf{P}_{\tilde{\mathbf{a}}}\tilde{\mathbf{X}}\mathbf{w}_d^*\mathbf{w}_d^T\right)}{\hat{\gamma}_1}\right]} \underset{H_0}{\overset{H_1}{\gtrless}} \lambda'_{OGLRT-PHE}. \tag{27}$$

3.2. TGLRT

In this subsection, we investigate the TGLRT criterion to address the detection problem proposed earlier. First, we derive the GLRT using a deterministic and known matrix $\mathbf{R}$. Then, we replace $\mathbf{R}$ in the GLRT derived above with the training data SCM $\mathbf{S}/(KL)$.

The GLRT for the known $\mathbf{R}$ is given by [37]

$$\Lambda_{TGLRT-PHE} = \frac{\max\limits_{\alpha_s, \gamma} f\left(\mathbf{X}, \mathbf{Y}|\alpha_s, \gamma, \mathbf{R}, H_1\right)}{\max\limits_{\gamma} f\left(\mathbf{X}, \mathbf{Y}|\gamma, \mathbf{R}, H_0\right)} \underset{H_0}{\overset{H_1}{\gtrless}} \lambda_{TGLRT-PHE}, \tag{28}$$

where $\lambda_{TGLRT-PHE}$ is the detection threshold. Deriving the derivative of the logarithm of (14) regarding γ leads to

$$\frac{\partial \ln f(\mathbf{X},\mathbf{Y}|\alpha_s,\gamma,\mathbf{R},H_1)}{\partial \gamma} = -\frac{MNK}{\gamma} + \frac{tr(\mathbf{R}^{-1}\mathbf{X}_{\alpha_s}\mathbf{X}_{\alpha_s}^H)}{\gamma^2}. \tag{29}$$

Setting $\frac{\partial \ln f(\mathbf{X},\mathbf{Y}|\alpha_s,\gamma,\mathbf{R},H_1)}{\partial \gamma} = 0$, we obtain the MLE of γ under H_1 as

$$\hat{\gamma}_1 = \frac{tr(\mathbf{R}^{-1}\mathbf{X}_{\alpha_s}\mathbf{X}_{\alpha_s}^H)}{MNK}. \tag{30}$$

Inserting (30) into (14) yields

$$f(\mathbf{X},\mathbf{Y}|\alpha_s,\hat{\gamma}_1,\mathbf{R},H_1) = \frac{\varepsilon}{tr^{MNK}(\mathbf{R}^{-1}\mathbf{X}_{\alpha_s}\mathbf{X}_{\alpha_s}^H)}, \tag{31}$$

where $\varepsilon = \frac{(MNK)^{MNK}e^{-MNK-tr(\mathbf{R}^{-1}\mathbf{S})}}{\pi^{MNK(L+1)}\det^{K(L+1)}(\mathbf{R})}$ denotes a parameter without unknown variables α_s and γ. Furthermore, we define

$$g(\alpha_s) = tr\left(\mathbf{R}^{-1}\mathbf{X}_{\alpha_s}\mathbf{X}_{\alpha_s}^H\right), \tag{32}$$

which appears in (30) and (31) simultaneously. The derivative of (32) regarding α_s leads to

$$\frac{\partial g(\alpha_s)}{\partial \alpha_s} = -\mathbf{w}_d^T\mathbf{X}_{\alpha_s}^H\mathbf{R}^{-1}\mathbf{a}_{tr} = -\mathbf{w}_d^T\left(\mathbf{X} - \alpha_s\mathbf{a}_{tr}\mathbf{w}_d^T\right)^H\mathbf{R}^{-1}\mathbf{a}_{tr}. \tag{33}$$

Equation (33) to zero gives the MLE of α_s as

$$\hat{\alpha}_s = \frac{\mathbf{a}_{tr}^H\mathbf{R}^{-1}\mathbf{X}\mathbf{w}_d^*}{\mathbf{a}_{tr}^H\mathbf{R}^{-1}\mathbf{a}_{tr}}, \tag{34}$$

where the fact $\mathbf{w}_d^T\mathbf{w}_d^* = 1$ is applied. Plugging (34) into (32), we obtain

$$g(\hat{\alpha}_s) = tr\left(\mathbf{X}^H\mathbf{R}^{-1}\mathbf{X}\right) - \frac{\left|\mathbf{a}_{tr}^H\mathbf{R}^{-1}\mathbf{X}\mathbf{w}_d^*\right|^2}{\mathbf{a}_{tr}^H\mathbf{R}^{-1}\mathbf{a}_{tr}}. \tag{35}$$

where symbol $|\cdot|$ denotes modulus of a complex number. It is worth noting that (35) can also be interpreted as an estimate of $\hat{\gamma}_1$, which neglects constants and has no unknown variables.

Similar to (30), the MLE of γ under H_0 can be obtained as

$$\hat{\gamma}_0 = \frac{tr(\mathbf{R}^{-1}\mathbf{X}\mathbf{X}^H)}{MNK}. \tag{36}$$

Then, we can simplify (13) by applying (36) as follows

$$f(\mathbf{X},\mathbf{Y}|\hat{\gamma}_0,\mathbf{R},H_0) = \frac{\varepsilon}{tr^{MNK}(\mathbf{R}^{-1}\mathbf{X}\mathbf{X}^H)}. \tag{37}$$

After substituting (31), (35) and (37) into (28) and taking the MNKth root and performing algebraic operations, we can obtain

$$\Lambda'_{TGLRT-PHE} = \frac{tr(\mathbf{R}^{-1}\mathbf{X}\mathbf{X}^H)}{tr(\mathbf{X}^H\mathbf{R}^{-1}\mathbf{X}) - \frac{\left|\mathbf{a}_{tr}^H\mathbf{R}^{-1}\mathbf{X}\mathbf{w}_d^*\right|^2}{\mathbf{a}_{tr}^H\mathbf{R}^{-1}\mathbf{a}_{tr}\mathbf{w}_d^T\mathbf{w}_d^*}} \underset{H_0}{\overset{H_1}{\gtrless}} \lambda_{TGLRT-PHE}'. \tag{38}$$

where $\lambda'_{TGLRT-PHE}$ denotes a modification of the threshold in (28).

As a matter of fact, in practice, (38) is not feasible due to the presence of an unknown noise covariance matrix (NCM). Hence, we use SCM $\mathbf{S}/(KL)$ to replace $\mathbf{R}$ to obtain the final TGLRT detector independent of $\mathbf{R}$ as

$$\Lambda'_{TGLRT-PHE} = \frac{tr(\tilde{\mathbf{X}}^H\tilde{\mathbf{X}})}{tr(\tilde{\mathbf{X}}^H\tilde{\mathbf{X}}) - \frac{|\tilde{\mathbf{a}}^H\tilde{\mathbf{X}}\mathbf{w}_d^*|^2}{\tilde{\mathbf{a}}^H\tilde{\mathbf{a}}}} \underset{H_0}{\overset{H_1}{\gtrless}} \lambda_{TGLRT-PHE}'. \tag{39}$$

3.3. TRao Test

Let $\boldsymbol{\theta}$ be a parameter vector, expressed as

$$\boldsymbol{\theta} = \left[\boldsymbol{\theta}_r^T, \boldsymbol{\theta}_s^T\right]^T, \tag{40}$$

where $\boldsymbol{\theta}_r = \alpha_s \in \mathbb{C}^{1\times1}$ contains a useful argument, and $\boldsymbol{\theta}_s = \left[\gamma, \text{vec}^T(\mathbf{R})\right]^T \in \mathbb{C}^{(1+M^2N^2)\times1}$ contains redundant arguments with symbol $\text{vec}(\cdot)$ denoting vectorization. The Fisher information matrix (FIM) can be partitioned as

$$\mathbf{F}(\boldsymbol{\theta}) = \begin{bmatrix} \mathbf{F}_{\boldsymbol{\theta_r},\boldsymbol{\theta_r}}(\boldsymbol{\theta}) & \mathbf{F}_{\boldsymbol{\theta_r},\boldsymbol{\theta_s}}(\boldsymbol{\theta}) \\ \mathbf{F}_{\boldsymbol{\theta_s},\boldsymbol{\theta_r}}(\boldsymbol{\theta}) & \mathbf{F}_{\boldsymbol{\theta_s},\boldsymbol{\theta_s}}(\boldsymbol{\theta}) \end{bmatrix}, \tag{41}$$

or equivalently expressed as

$$\mathbf{F}(\boldsymbol{\theta}) = \text{E}\left[\left(\frac{\partial \ln f(\mathbf{X},\mathbf{Y}|\alpha_s,\gamma,\mathbf{R},H_1)}{\partial\boldsymbol{\theta}^*}\right)\left(\frac{\partial \ln f(\mathbf{X},\mathbf{Y}|\alpha_s,\gamma,\mathbf{R},H_1)}{\partial\boldsymbol{\theta}^T}\right)\right], \tag{42}$$

where

$$\begin{aligned}\mathbf{F}_{\boldsymbol{\theta}_i,\boldsymbol{\theta}_j}(\boldsymbol{\theta}) &= -\text{E}\left[\frac{\partial^2 \ln f(\mathbf{X},\mathbf{Y}|\alpha_s,\gamma,\mathbf{R},H_1)}{\partial\boldsymbol{\theta}_i^*\partial\boldsymbol{\theta}_j^T}\right] i,j \in (r,s) \\ &= \text{E}\left[\left(\frac{\partial \ln f(\mathbf{X},\mathbf{Y}|\alpha_s,\gamma,\mathbf{R},H_1)}{\partial\boldsymbol{\theta}_i^*}\right)\left(\frac{\partial \ln f(\mathbf{X},\mathbf{Y}|\alpha_s,\gamma,\mathbf{R},H_1)}{\partial\boldsymbol{\theta}_j^T}\right)\right],\end{aligned} \tag{43}$$

with symbol $\text{E}(\cdot)$ denoting the statistical expectation. Next, the Rao test with known $\mathbf{R}$ is expressed as [40]

$$\Lambda_{TRao-PHE} = \left.\frac{\partial \ln f(\mathbf{X},\mathbf{Y}|\alpha_s,\gamma,\mathbf{R},H_1)}{\partial\boldsymbol{\theta}_r}\right|^T_{\boldsymbol{\theta}=\hat{\boldsymbol{\theta}}_0} \left[\mathbf{F}^{-1}(\hat{\boldsymbol{\theta}}_0)\right]_{\boldsymbol{\theta}_r,\boldsymbol{\theta}_r} \tag{44}$$

$$\left.\frac{\partial \ln f(\mathbf{X},\mathbf{Y}|\alpha_s,\gamma,\mathbf{R},H_1)}{\partial\boldsymbol{\theta}_r^*}\right|_{\boldsymbol{\theta}=\hat{\boldsymbol{\theta}}_0} \underset{H_0}{\overset{H_1}{\gtrless}} \lambda_{TRao-PHE}$$

with $\hat{\boldsymbol{\theta}}_0 = \left[\boldsymbol{\theta}_{r0}^T, \boldsymbol{\theta}_{s0}^T\right]^T$ being the MLE of $\boldsymbol{\theta}$ under hypothesis H_0. $\lambda_{TRao-PHE}$ is the detection threshold. Moreover, according to Schur complement theorem, $\left[\mathbf{F}^{-1}(\boldsymbol{\theta})\right]_{\boldsymbol{\theta}_r,\boldsymbol{\theta}_r}$ can be written as

$$\left[\mathbf{F}^{-1}(\boldsymbol{\theta})\right]_{\boldsymbol{\theta}_r,\boldsymbol{\theta}_r} = \left[\mathbf{F}_{\boldsymbol{\theta}_r,\boldsymbol{\theta}_r}(\boldsymbol{\theta}) - \mathbf{F}_{\boldsymbol{\theta}_r,\boldsymbol{\theta}_s}(\boldsymbol{\theta})\mathbf{F}_{\boldsymbol{\theta}_s,\boldsymbol{\theta}_s}^{-1}(\boldsymbol{\theta})\mathbf{F}_{\boldsymbol{\theta}_s,\boldsymbol{\theta}_r}(\boldsymbol{\theta})\right]^{-1}. \tag{45}$$

As for the partial derivative parts in (44), derivatizing the logarithm of (14) regarding $\boldsymbol{\theta}_r$ and $\boldsymbol{\theta}_r^*$, respectively, produces

$$\frac{\partial \ln f(\mathbf{X},\mathbf{Y}|\alpha_s,\gamma,\mathbf{R},H_1)}{\partial\boldsymbol{\theta}_r} = \frac{\partial \ln f(\mathbf{X},\mathbf{Y}|\alpha_s,\gamma,\mathbf{R},H_1)}{\partial\alpha_s} = \mathbf{w}_d^T\left(\mathbf{X} - \alpha_s\mathbf{a}_{tr}\mathbf{w}_d^T\right)^H\mathbf{R}^{-1}\mathbf{a}_{tr}/\gamma, \tag{46}$$

and

$$\frac{\partial \ln f(\mathbf{X},\mathbf{Y}|\alpha_s,\gamma,\mathbf{R},H_1)}{\partial\boldsymbol{\theta}_r^*} = \frac{\partial \ln f(\mathbf{X},\mathbf{Y}|\alpha_s,\gamma,\mathbf{R},H_1)}{\partial\alpha_s^*} = \mathbf{a}_{tr}^H\mathbf{R}^{-1}\left(\mathbf{X} - \alpha_s\mathbf{a}_{tr}\mathbf{w}_d^T\right)\mathbf{w}_d^*/\gamma. \tag{47}$$

Substituting (46) and (47) into the second equation in (43), and equating α_s to zero, result in

$$\mathbf{F}_{\theta_r,\theta_r}(\hat{\boldsymbol{\theta}}_0) = \mathbf{a}_{tr}^H \mathbf{R}^{-1} \mathrm{E}\left(\mathbf{X}\mathbf{w}_d^* \mathbf{w}_d^T \mathbf{X}^H\right) \mathbf{R}^{-1} \mathbf{a}_{tr}/\hat{\gamma}_0^2 = \mathbf{w}_d^T \mathbf{w}_d^* \mathbf{a}_{tr}^H \mathbf{R}^{-1} \mathbf{a}_{tr}/\hat{\gamma}_0 = \mathbf{a}_{tr}^H \mathbf{R}^{-1} \mathbf{a}_{tr}/\hat{\gamma}_0. \quad (48)$$

Moreover, according to the first equation in (43), taking the derivative of (47) regarding $\boldsymbol{\theta}_s^T$ and performing the expectation yield

$$
\begin{aligned}
\mathbf{F}_{\theta_r,\theta_s}(\boldsymbol{\theta}) &= -\mathrm{E}\left[\frac{\partial^2 \ln f(\mathbf{X},\mathbf{Y}|\alpha_s,\gamma,\mathbf{R},H_1)}{\partial \boldsymbol{\theta}_r^* \partial \boldsymbol{\theta}_s^T}\right] \\
&= -\mathrm{E}\left\{\frac{\partial \left(\mathbf{a}_{tr}^H \mathbf{R}^{-1} \mathbf{X}_{\alpha_s} \mathbf{w}_d^*/\gamma\right)}{\partial \gamma}, \mathrm{vec}^T\left[\frac{\partial \left(\mathbf{a}_{tr}^H \mathbf{R}^{-1} \mathbf{X}_{\alpha_s} \mathbf{w}_d^*/\gamma\right)}{\partial \mathbf{R}}\right]\right\} \\
&= \mathrm{E}\left[\frac{\mathbf{a}_{tr}^H \mathbf{R}^{-1} \mathbf{X}_{\alpha_s} \mathbf{w}_d^*}{\gamma^2}, \mathrm{vec}^T\left(\frac{\mathbf{R}^{-1} \mathbf{X}_{\alpha_s} \mathbf{w}_d^* \mathbf{a}_{tr}^H \mathbf{R}^{-1}}{\gamma}\right)\right] \\
&= \left\{\frac{\mathbf{a}_{tr}^H \mathbf{R}^{-1} \mathrm{E}(\mathbf{X}_{\alpha_s}) \mathbf{w}_d^*}{\gamma^2}, \mathrm{vec}^T\left[\frac{\mathbf{R}^{-1} \mathrm{E}(\mathbf{X}_{\alpha_s}) \mathbf{w}_d^* \mathbf{a}_{tr}^H \mathbf{R}^{-1}}{\gamma}\right]\right\} \\
&= \mathbf{0}_{1\times(M^2N^2+1)}.
\end{aligned}
\quad (49)
$$

Plugging (48) and (49) to (45), yields

$$\left[\mathbf{F}^{-1}(\hat{\boldsymbol{\theta}}_0)\right]_{\theta_r,\theta_r} = \left[\mathbf{F}_{\theta_r,\theta_r}(\hat{\boldsymbol{\theta}}_0)\right]^{-1} = \hat{\gamma}_0 \left(\mathbf{a}_{tr}^H \mathbf{R}^{-1} \mathbf{a}_{tr}\right)^{-1}. \quad (50)$$

Applying (46), (47) and (50) to (44) and setting α_s to zero yield the Rao test for the known $\mathbf{R}$ as

$$\Lambda_{TRao-PHE} = \frac{\left|\mathbf{a}_{tr}^H \mathbf{R}^{-1} \mathbf{X}^H \mathbf{w}_d^*\right|^2}{\hat{\gamma}_0 \mathbf{a}_{tr}^H \mathbf{R}^{-1} \mathbf{a}_{tr}}. \quad (51)$$

Substitute $\hat{\gamma}_0$ in (36) into (51) and replace $\mathbf{R}$ with SCM $\mathbf{S}/(KL)$, we obtain the final TRao test by ignoring the constant term as

$$\Lambda'_{TRao-PHE} = \frac{\left|\tilde{\mathbf{a}}^H \tilde{\mathbf{X}} \mathbf{w}_d^*\right|^2}{tr\left(\tilde{\mathbf{X}}^H \tilde{\mathbf{X}}\right) \tilde{\mathbf{a}}^H \tilde{\mathbf{a}}} \underset{H_0}{\overset{H_1}{\gtrless}} \lambda'_{TRao-PHE}, \quad (52)$$

where $\lambda'_{TRao-PHE}$ denotes a modification of the threshold in (44).

3.4. TWald Test

The Wald test with known $\mathbf{R}$ is expressed is [40]

$$\Lambda_{TWald-PHE} = \left(\hat{\boldsymbol{\theta}}_{r1} - \boldsymbol{\theta}_{r0}\right)^H \left\{\left[\mathbf{F}^{-1}(\hat{\boldsymbol{\theta}}_1)\right]_{\theta_r,\theta_r}\right\}^{-1} \left(\hat{\boldsymbol{\theta}}_{r1} - \boldsymbol{\theta}_{r0}\right) \underset{H_0}{\overset{H_1}{\gtrless}} \lambda_{TWald-PHE}, \quad (53)$$

where $\hat{\boldsymbol{\theta}}_{r1}$ and $\hat{\boldsymbol{\theta}}_1$ are the MLEs of $\boldsymbol{\theta}_r$ and $\boldsymbol{\theta}$ under hypothesis H_1, respectively. $\boldsymbol{\theta}_{r0}$ is the value of $\boldsymbol{\theta}_r$ under hypothesis H_0. $\left\{\left[\mathbf{F}^{-1}(\boldsymbol{\theta})\right]_{\theta_r,\theta_r}\right\}^{-1}$, the Schur complement of $\mathbf{F}_{\theta_s,\theta_s}(\boldsymbol{\theta})$, is expressed in the form of the inversion of (45). $\lambda_{TWald-PHE}$ is the detection threshold.

For the intermediate term in (53), in the manner analogous to (48), we obtain

$$\mathbf{F}_{\theta_r,\theta_r}(\hat{\boldsymbol{\theta}}_1) = \frac{\mathbf{a}_{tr}^H \mathbf{R}^{-1} \mathbf{a}_{tr}}{\hat{\gamma}_1}. \quad (54)$$

Furthermore, we have

$$\left\{ \left[\mathbf{F}^{-1}\left(\hat{\boldsymbol{\theta}}_1 \right) \right]_{\boldsymbol{\theta}_r, \boldsymbol{\theta}_r} \right\}^{-1} = \mathbf{a}_{tr}^H \mathbf{R}^{-1} \mathbf{a}_{tr} / \hat{\gamma}_1 \tag{55}$$

Inserting (34) and (55) into (53) yields the Wald test for the known $\mathbf{R}$ as

$$\Lambda'_{TWald-PHE} = \frac{\left| \mathbf{a}_{tr}^H \mathbf{R}^{-1} \mathbf{X} \mathbf{w}_d^* \right|^2}{\mathbf{a}_{tr}^H \mathbf{R}^{-1} \mathbf{a}_{tr} \hat{\gamma}_1} \underset{H_0}{\overset{H_1}{\gtrless}} \lambda'_{TWald-PHE} \tag{56}$$

where $\lambda'_{TWald-PHE}$ denotes a modification of the threshold in (53).

Plugging $\hat{\gamma}_1$ in (35) into (56) and replacing $\mathbf{R}$ with SCM $\mathbf{S}/(KL)$, we can derive the final TWald test as

$$\Lambda'_{TWald-PHE} = \frac{\left| \tilde{\mathbf{a}}^H \tilde{\mathbf{X}} \mathbf{w}_d^* \right|^2}{\tilde{\mathbf{a}}^H \tilde{\mathbf{a}} tr\left(\tilde{\mathbf{X}}^H \tilde{\mathbf{X}} \right) - \left| \tilde{\mathbf{a}}^H \tilde{\mathbf{X}} \mathbf{w}_d^* \right|^2} \underset{H_0}{\overset{H_1}{\gtrless}} \lambda'_{TWald-PHE}. \tag{57}$$

4. Analysis of CFAR Property

As one of the crucial features of the adaptive detectors, the CFAR property has become a vital requirement. In this section, we refer to the analysis presented in the literature [30,39,41] to demonstrate that the detectors proposed in (27), (39), (52) and (57) possess the CFAR property due to their irrelevance to the noise covariance matrix $\mathbf{R}$ and the scaling factor γ.

We first analyze the CFAR property of the OGLRT-PHE detector in (27). Please note that the term $\left(\tilde{\mathbf{X}} - \mathbf{P}_{\tilde{\mathbf{a}}} \tilde{\mathbf{X}} \mathbf{w}_d^* \mathbf{w}_d^T \right)^H \left(\tilde{\mathbf{X}} - \mathbf{P}_{\tilde{\mathbf{a}}} \tilde{\mathbf{X}} \mathbf{w}_d^* \mathbf{w}_d^T \right)$ in the denominator can be rewritten as

$$
\begin{aligned}
&\left(\tilde{\mathbf{X}} - \mathbf{P}_{\tilde{\mathbf{a}}} \tilde{\mathbf{X}} \mathbf{w}_d^* \mathbf{w}_d^T \right)^H \left(\tilde{\mathbf{X}} - \mathbf{P}_{\tilde{\mathbf{a}}} \tilde{\mathbf{X}} \mathbf{w}_d^* \mathbf{w}_d^T \right) \\
&= \tilde{\mathbf{X}}^H \tilde{\mathbf{X}} - \tilde{\mathbf{X}}^H \mathbf{P}_{\tilde{\mathbf{a}}} \tilde{\mathbf{X}} \mathbf{w}_d^* \mathbf{w}_d^T - \mathbf{w}_d^* \mathbf{w}_d^T \tilde{\mathbf{X}}^H \mathbf{P}_{\tilde{\mathbf{a}}} \tilde{\mathbf{X}} + \mathbf{w}_d^* \mathbf{w}_d^T \tilde{\mathbf{X}}^H \mathbf{P}_{\tilde{\mathbf{a}}} \tilde{\mathbf{X}} \mathbf{w}_d^* \mathbf{w}_d^T \\
&= \left(\tilde{\mathbf{X}}^H \tilde{\mathbf{X}} - \tilde{\mathbf{X}}^H \mathbf{P}_{\tilde{\mathbf{a}}} \tilde{\mathbf{X}} \right) + \left(\tilde{\mathbf{X}}^H \mathbf{P}_{\tilde{\mathbf{a}}} \tilde{\mathbf{X}} - \tilde{\mathbf{X}}^H \mathbf{P}_{\tilde{\mathbf{a}}} \tilde{\mathbf{X}} \mathbf{w}_d^* \mathbf{w}_d^T \right) - \left(\mathbf{w}_d^* \mathbf{w}_d^T \tilde{\mathbf{X}}^H \mathbf{P}_{\tilde{\mathbf{a}}} \tilde{\mathbf{X}} - \mathbf{w}_d^* \mathbf{w}_d^T \tilde{\mathbf{X}}^H \mathbf{P}_{\tilde{\mathbf{a}}} \tilde{\mathbf{X}} \mathbf{w}_d^* \mathbf{w}_d^T \right) \\
&= \tilde{\mathbf{X}}^H \tilde{\mathbf{X}} - \tilde{\mathbf{X}}^H \mathbf{P}_{\tilde{\mathbf{a}}} \tilde{\mathbf{X}} + \mathbf{P}_{\mathbf{w}_d^*}^\perp \tilde{\mathbf{X}}^H \mathbf{P}_{\tilde{\mathbf{a}}} \tilde{\mathbf{X}} \mathbf{P}_{\mathbf{w}_d^*}^\perp,
\end{aligned} \tag{58}
$$

where $\mathbf{P}_{\mathbf{w}_d^*}^\perp = \mathbf{I}_K - \mathbf{P}_{\mathbf{w}_d^*}$ with $\mathbf{P}_{\mathbf{w}_d^*} = \mathbf{w}_d^* \mathbf{w}_d^T$ being the projection matrix onto the column space of $\mathbf{w}_d^*$.

The first term in (58) is equivalent to

$$\tilde{\mathbf{X}}^H \tilde{\mathbf{X}} = \mathbf{X}^H \mathbf{S}^{-1} \mathbf{X} = \widehat{\mathbf{X}}^H \widehat{\mathbf{S}}_I^{-1} \widehat{\mathbf{X}} = \gamma \widehat{\mathbf{X}}_I^H \widehat{\mathbf{S}}_I^{-1} \widehat{\mathbf{X}}_I, \tag{59}$$

where $\widehat{\mathbf{X}} = \mathbf{R}^{-1/2} \mathbf{X}$, $\widehat{\mathbf{S}}_I = \mathbf{R}^{-1/2} \mathbf{S} \mathbf{R}^{-1/2}$ and $\widehat{\mathbf{X}}_I = \widehat{\mathbf{X}} / \sqrt{\gamma}$. At this point, we can observe that under hypothesis H_0, each column of $\widehat{\mathbf{X}}_I$ follows a zero-mean complex circular Gaussian distribution with covariance matrix $\mathbf{I}_{MN}$, i.e., $\widehat{\mathbf{X}}_I \sim \mathrm{CN}(0, \mathbf{I}_{MN} \otimes \mathbf{I}_K)$. At the same time, $\widehat{\mathbf{S}}_I$ follows an LK-degree-of-freedom complex central Wishart distribution with associated covariance matrix $\mathbf{I}_{MN}$ [42], i.e., $\widehat{\mathbf{S}}_I \sim \mathrm{W}(LK, \mathbf{I}_{MN})$. As a result, $\widehat{\mathbf{X}}_I$ and $\widehat{\mathbf{S}}_I$ are independent of $\mathbf{R}$ and γ.

The last two terms in (58) both contain $\tilde{\mathbf{X}}^H \mathbf{P}_{\tilde{\mathbf{a}}} \tilde{\mathbf{X}}$, which can be recast as

$$\tilde{\mathbf{X}}^H \mathbf{P}_{\tilde{\mathbf{a}}} \tilde{\mathbf{X}} = \frac{\mathbf{X}^H \mathbf{S}^{-1} \mathbf{a}_{tr} \mathbf{a}_{tr}^H \mathbf{S}^{-1} \mathbf{X}}{\mathbf{a}_{tr}^H \mathbf{S}^{-1} \mathbf{a}_{tr}} = \frac{\widehat{\mathbf{X}}^H \widehat{\mathbf{S}}_I^{-1} \widehat{\mathbf{a}}_{tr} \widehat{\mathbf{a}}_{tr}^H \widehat{\mathbf{S}}_I^{-1} \widehat{\mathbf{X}}}{\widehat{\mathbf{a}}_{tr}^H \widehat{\mathbf{S}}_I^{-1} \widehat{\mathbf{a}}_{tr}} = \frac{\gamma \widehat{\mathbf{X}}_I^H \widehat{\mathbf{S}}_I^{-1} \widehat{\mathbf{a}}_{tr} \widehat{\mathbf{a}}_{tr}^H \widehat{\mathbf{S}}_I^{-1} \widehat{\mathbf{X}}_I}{\widehat{\mathbf{a}}_{tr}^H \widehat{\mathbf{S}}_I^{-1} \widehat{\mathbf{a}}_{tr}}, \tag{60}$$

where $\widehat{\mathbf{a}}_{tr} = \mathbf{R}^{-1/2}\mathbf{a}_{tr}$. Please note that $\widehat{\mathbf{a}}_{tr} \in \mathbb{C}^{MN \times 1}$ is a full-column-rank matrix, and after orthogonal triangular decomposition, it can be expressed as

$$\widehat{\mathbf{a}}_{tr} = a\mathbf{U}_s, \tag{61}$$

where $a \in \mathbb{C}^{1 \times 1}$ is a non-zero scalar, and sub-unitary matrix $\mathbf{U}_s \in \mathbb{C}^{MN \times 1}$ is equivalent to the first column of an unitary matrix $\mathbf{U} \in \mathbb{C}^{MN \times MN}$, with $\mathbf{I}_a = \mathbf{U}^H \mathbf{U}_s = \begin{bmatrix} 1 & \mathbf{0}_{1 \times (MN-1)} \end{bmatrix}^T \in \mathbb{C}^{MN \times 1}$. In this way, (60) can be further transformed to

$$\tilde{\mathbf{X}}^H \mathbf{P}_{\tilde{\mathbf{a}}} \tilde{\mathbf{X}} = \frac{\gamma \mathbf{Z}^H \mathbf{Q}^{-1} \left(\mathbf{U}^H \widehat{\mathbf{a}}_{tr}\right)\left(\mathbf{U}^H \widehat{\mathbf{a}}_{tr}\right)^H \mathbf{Q}^{-1} \mathbf{Z}}{\left(\mathbf{U}^H \widehat{\mathbf{a}}_{tr}\right)^H \mathbf{Q}^{-1} \left(\mathbf{U}^H \widehat{\mathbf{a}}_{tr}\right)} = \frac{\gamma \mathbf{Z}^H \mathbf{Q}^{-1} \mathbf{I}_a \mathbf{I}_a^H \mathbf{Q}^{-1} \mathbf{Z}}{\mathbf{I}_a^H \mathbf{Q}^{-1} \mathbf{I}_a}, \tag{62}$$

where $\mathbf{Z} = \mathbf{U}^H \widehat{\mathbf{X}}_I$ and $\mathbf{Q} = \mathbf{U}^H \widehat{\mathbf{S}}_I \mathbf{U}$. Please note that under hypothesis H_0, $\mathbf{Z}$ and $\mathbf{Q}$ in (62) are statistically equivalent to $\widehat{\mathbf{X}}_I$ and $\widehat{\mathbf{S}}_I$ in (59), respectively. Hence, they are also uncorrelated with $\mathbf{R}$ and γ. To proceed with the proof, we partition the matrices $\mathbf{Z}$ and $\mathbf{Q}$ as needed. Let

$$\mathbf{Z} = \begin{bmatrix} \mathbf{Z}_1 \in \mathbb{C}^{1 \times K} \\ \mathbf{Z}_2 \in \mathbb{C}^{(MN-1) \times K} \end{bmatrix}, \tag{63}$$

$$\mathbf{Q} = \begin{bmatrix} Q_{11} \in \mathbb{C}^{1 \times 1} & \mathbf{Q}_{12} \in \mathbb{C}^{1 \times (MN-1)} \\ \mathbf{Q}_{21} \in \mathbb{C}^{(MN-1) \times 1} & \mathbf{Q}_{22} \in \mathbb{C}^{(MN-1) \times (MN-1)} \end{bmatrix}, \tag{64}$$

and

$$\mathbf{Q}^{-1} = \begin{bmatrix} Q^{11} \in \mathbb{C}^{1 \times 1} & \mathbf{Q}^{12} \in \mathbb{C}^{1 \times (MN-1)} \\ \mathbf{Q}^{21} \in \mathbb{C}^{(MN-1) \times 1} & \mathbf{Q}^{22} \in \mathbb{C}^{(MN-1) \times (MN-1)} \end{bmatrix} \tag{65}$$

with $Q^{11} = \left(Q_{11} - \mathbf{Q}_{12}\mathbf{Q}_{22}^{-1}\mathbf{Q}_{21}\right)^{-1}$ and $\mathbf{Q}^{12} = -\left(Q_{11} - \mathbf{Q}_{12}\mathbf{Q}_{22}^{-1}\mathbf{Q}_{21}\right)^{-1}\mathbf{Q}_{12}\mathbf{Q}_{22}^{-1} = -Q^{11} \times \mathbf{Q}_{12}\mathbf{Q}_{22}^{-1}$ according to the partitioned matrix inversion formula [43]. Since $\mathbf{Q}$ and $\mathbf{Q}^{-1}$ both are Hermitian matrices, i.e., $\mathbf{Q} = \mathbf{Q}^H$ and $\mathbf{Q}^{-1} = \left(\mathbf{Q}^{-1}\right)^H$, we have $\mathbf{Q}^{21} = \left(\mathbf{Q}^{12}\right)^H$. Then, (62) can be further reformulated as

$$\begin{aligned}
\tilde{\mathbf{X}}^H \mathbf{P}_{\tilde{\mathbf{a}}} \tilde{\mathbf{X}} &= \gamma \begin{bmatrix} \mathbf{Z}_1^H & \mathbf{Z}_2^H \end{bmatrix} \begin{bmatrix} Q^{11} \\ \mathbf{Q}^{21} \end{bmatrix} \begin{bmatrix} Q^{11} & \mathbf{Q}^{12} \end{bmatrix} \begin{bmatrix} \mathbf{Z}_1 \\ \mathbf{Z}_2 \end{bmatrix} \left(Q^{11}\right)^{-1} \\
&= \gamma \left(Q^{11}\right)^{-1} \begin{bmatrix} \mathbf{Z}_1^H & \mathbf{Z}_2^H \end{bmatrix} \begin{bmatrix} Q^{11} \\ \mathbf{Q}^{21} \end{bmatrix} Q^{11} \begin{bmatrix} Q^{11} & \mathbf{Q}^{12} \end{bmatrix} \begin{bmatrix} \mathbf{Z}_1 \\ \mathbf{Z}_2 \end{bmatrix} \left(Q^{11}\right)^{-1} \\
&= \gamma \left(Q^{11}\right)^{-1} \left[Q^{11}\mathbf{Z}_1 + \left(\mathbf{Q}^{21}\right)^H \mathbf{Z}_2\right]^H Q^{11} \left(Q^{11}\mathbf{Z}_1 + \mathbf{Q}^{12}\mathbf{Z}_2\right) \left(Q^{11}\right)^{-1} \\
&= \gamma \left(\mathbf{Z}_1 - \mathbf{Q}_{12}\mathbf{Q}_{22}^{-1}\mathbf{Z}_2\right)^H Q^{11} \left(\mathbf{Z}_1 - \mathbf{Q}_{12}\mathbf{Q}_{22}^{-1}\mathbf{Z}_2\right) \\
&= \gamma \mathbf{A}^H Q^{11} \mathbf{A}
\end{aligned} \tag{66}$$

where $\mathbf{A} = \mathbf{Z}_1 - \mathbf{Q}_{12}\mathbf{Q}_{22}^{-1}\mathbf{Z}_2$. Since $\mathbf{Z}$ and $\mathbf{Q}$ are independent on $\mathbf{R}$ and γ, $\mathbf{A}$ is also independent on $\mathbf{R}$ and γ.

In the same way, the term $\tilde{\mathbf{X}}^H \tilde{\mathbf{X}}$ in the numerator of (27) is also equivalent to (59). On the other hand, following the approach in [39], $\hat{\gamma}_0$ and $\hat{\gamma}_1$ in (27) can be recast as

$$\hat{\gamma}_0 = \gamma \iota_0, \tag{67}$$

and

$$\hat{\gamma}_1 = \gamma \iota_1, \tag{68}$$

respectively, where ι_0 and ι_1 are independent of $\mathbf{R}$ and γ. Plugging (58), (59), (66), (67) and (68) into (27) results in

$$
\Lambda'_{OGLRT-PHE} = \frac{\iota_0^{\frac{MN}{L+1}} \det\left[\mathbf{I}_K + \frac{\widehat{\mathbf{X}}_I^{\,H} \widehat{\mathbf{S}}_I^{\,-1} \widehat{\mathbf{X}}_I}{\iota_0} \right]}{\iota_1^{\frac{MN}{L+1}} \det\left[\mathbf{I}_K + \frac{\widehat{\mathbf{X}}_I^{\,H} \widehat{\mathbf{S}}_I^{\,-1} \widehat{\mathbf{X}}_I - \mathbf{A}^H \mathbf{Q}^{11} \mathbf{A} + \mathbf{P}_{\mathbf{w}_d^*}^{\perp} \mathbf{A}^H \mathbf{Q}^{11} \mathbf{A} \mathbf{P}_{\mathbf{w}_d^*}^{\perp}}{\iota_1} \right]}.
\tag{69}
$$

Under hypothesis H_0, it can be inferred that $\widehat{\mathbf{X}}_I$, $\widehat{\mathbf{S}}_I$, $\mathbf{Q}$, $\mathbf{A}$ and $\iota_i, (i = 0, 1)$ are not related to $\mathbf{R}$ and γ. Therefore, the OGLRT-PHE detector exhibits the CFAR property against $\mathbf{R}$ and γ.

Furthermore, note that (39), (52) and (57) can all be expressed in the same form as

$$
\Lambda = \frac{\left| \tilde{\mathbf{a}}^H \tilde{\mathbf{X}} \mathbf{w}_d^* \right|^2}{\tilde{\mathbf{a}}^H \tilde{\mathbf{a}}\, \mathrm{tr}(\tilde{\mathbf{X}}^H \tilde{\mathbf{X}})} = \frac{\mathbf{w}_d^T \tilde{\mathbf{X}}^H \tilde{\mathbf{a}} \tilde{\mathbf{a}}^H \tilde{\mathbf{X}} \mathbf{w}_d^*}{\tilde{\mathbf{a}}^H \tilde{\mathbf{a}}\, \mathrm{tr}(\tilde{\mathbf{X}}^H \tilde{\mathbf{X}})} = \frac{\mathrm{tr}\left(\mathbf{w}_d^T \tilde{\mathbf{X}}^H \mathbf{P}_{\tilde{\mathbf{a}}} \tilde{\mathbf{X}} \mathbf{w}_d^* \right)}{\mathrm{tr}(\tilde{\mathbf{X}}^H \tilde{\mathbf{X}})}
$$

$$
= \frac{\mathrm{tr}\left(\mathbf{w}_d^* \mathbf{w}_d^T \tilde{\mathbf{X}}^H \mathbf{P}_{\tilde{\mathbf{a}}} \tilde{\mathbf{X}} \mathbf{w}_d^* \mathbf{w}_d^T \right)}{\mathrm{tr}(\tilde{\mathbf{X}}^H \tilde{\mathbf{X}})} = \frac{\mathrm{tr}\left(\mathbf{P}_{\mathbf{w}_d^*} \tilde{\mathbf{X}}^H \mathbf{P}_{\tilde{\mathbf{a}}} \tilde{\mathbf{X}} \mathbf{P}_{\mathbf{w}_d^*} \right)}{\mathrm{tr}(\tilde{\mathbf{X}}^H \tilde{\mathbf{X}})}.
\tag{70}
$$

Inserting (59) and (66) into above expression, we obtain

$$
\Lambda = \frac{\mathrm{tr}\left(\mathbf{P}_{\mathbf{w}_d^*} \tilde{\mathbf{X}}^H \mathbf{P}_{\tilde{\mathbf{a}}} \tilde{\mathbf{X}} \mathbf{P}_{\mathbf{w}_d^*} \right)}{\mathrm{tr}(\tilde{\mathbf{X}}^H \tilde{\mathbf{X}})} = \frac{\mathrm{tr}\left(\mathbf{P}_{\mathbf{w}_d^*} \mathbf{A}^H \mathbf{Q}^{11} \mathbf{A} \mathbf{P}_{\mathbf{w}_d^*} \right)}{\mathrm{tr}\left(\widehat{\mathbf{X}}_I^{\,H} \widehat{\mathbf{S}}_I^{\,-1} \widehat{\mathbf{X}}_I \right)}.
\tag{71}
$$

Clearly from the derivation above, we conclude that the TGLRT-PHE, the TRao-PHE, and the TWald-PHE detectors posses the property of CFAR.

5. Simulation Results

In this section, we conduct extensive numerical simulations to evaluate the performance of the proposed detectors based on the FDA-MIMO radar. For all simulations, we assume the radar operates at $f_0 = 10\,\mathrm{GHz}$, mounted with 3 transmit antennas and 4 receive antennas. The inter-element spacings are $d_T = d_R = c/(2f_0)$, and the bandwidth is $B = 1$ MHz. Unless stated otherwise, $K = 4$, $L = 6$, $\Delta f = 1$ MHz, and $\gamma = 3.2$. Due to the presence of thermal noise, mainlobe deceptive jamming, and range-compensated clutter in the scenario, the covariance matrix $\mathbf{R}$ can be modeled as

$$
\mathbf{R} = \sigma_n^2 \left(\mathbf{R}_n + \sum_j \xi_{jam,j} \mathbf{R}_j \right),
\tag{72}
$$

where σ_n^2 is noise (including clutter) power, generated deterministically according to the signal-to-noise ratio (SNR) defined as $\xi_n = 10\log_{10}\frac{|\alpha_s|^2}{\sigma_n^2}$. $\xi_{jam,j}$ is the jamming-to-noise ratio (JNR) of the jth deceptive jamming, defined as $\xi_{jam,j} = 10\log_{10}\frac{\sigma_{jam,j}^2}{\sigma_n^2}$ with $\sigma_{jam,j}^2$ is the power of the jth deceptive jamming. Moreover, the covariances of noise and deceptive jamming can be modeled as

$$
\mathbf{R}_n(i, j) = \rho^{|i-j|},
\tag{73}
$$

and

$$
\mathbf{R}_j = \mathbf{a}_{tr}(r_j, \theta_j) \mathbf{a}_{tr}^H(r_j, \theta_j),
\tag{74}
$$

respectively. In the simulation environment, we set $j = 2$, $\xi_{jam,j} = 15$ dB, and $\rho = 0.9$.

In addition, the detection thresholds and probabilities of detection (PDs) are obtained through the MC techniques, based on $100/PFA$ and 10^4 trials, respectively. PFA represents the probability of a false alarm, which is set to $PFA = 10^{-3}$.

Figure 1 illustrates the detection thresholds of proposed detectors in various cases of power mismatch γ and ρ, respectively. We can find that the detection thresholds of proposed detectors are less affected by the changes in γ and ρ, which confirms that the four detectors have CFAR property against γ and $\boldsymbol{R}$ in turn.
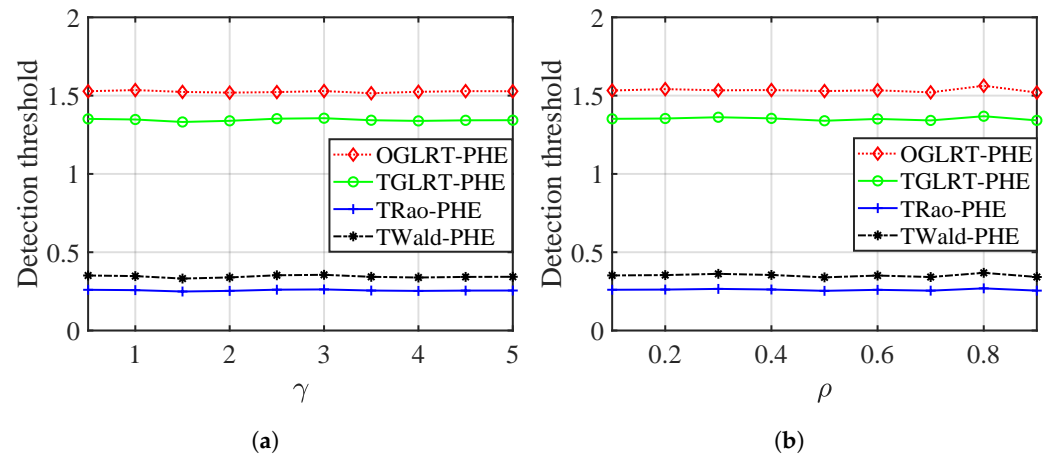
Figure 1. Detection threshold versus (**a**) γ and (**b**) ρ, respectively.

Figure 2 displays the detection performance of proposed detectors with different snapshots. In the legend, CD denotes the detector in (38) with a known covariance matrix **R**. Please note that this detector is impractical since it requires knowledge of the covariance matrix in advance. However, this ideal detector provides a useful performance constraint for any suboptimal method. Hence, it can be used to measure the performance of the proposed detectors. From Figure 2, it is evident that the OGLRT-PHE detector achieves a superior detection performance compared to the other three proposed detectors. This is because the OGLRT-PHE detector uses both the training and test data to estimate the covariance matrix **R**, which results in a more accurate estimation. The remaining three proposed detectors perform similarly as their detection statistics expressions are equivalent. Additionally, the larger the number of snapshots K, the better the performance of the proposed detectors, and the smaller the performance gaps between the proposed detectors and CD. Therefore, it can be predicted that when the number of snapshots K is large enough, the performance of all proposed detectors will be almost the same. This is because a larger number of snapshots leads to an increase in training data, which in turn provides a more reliable estimate of the covariance matrix **R**.

Figure 3 shows the detection performance of the proposed detectors with different sample covariance snapshots. It is observed that as we take more sample covariance snapshots L, the detectors' performance improves. This is consistent with the results obtained by increasing the number of snapshots K, as shown in Figure 2. The improvement is because increasing L and K provides more training data, which enhances the estimation precision of the covariance matrix **R**. However, there is a notable difference between Figures 2b and 3b. With the same amount of training data (the product of K and L is equal), increasing the number of snapshots K leads to significant improvement in detection performance. Moreover, Figure 3a illustrates that the proposed OGLRT-PHE detector outperforms other proposed detectors with less training data.
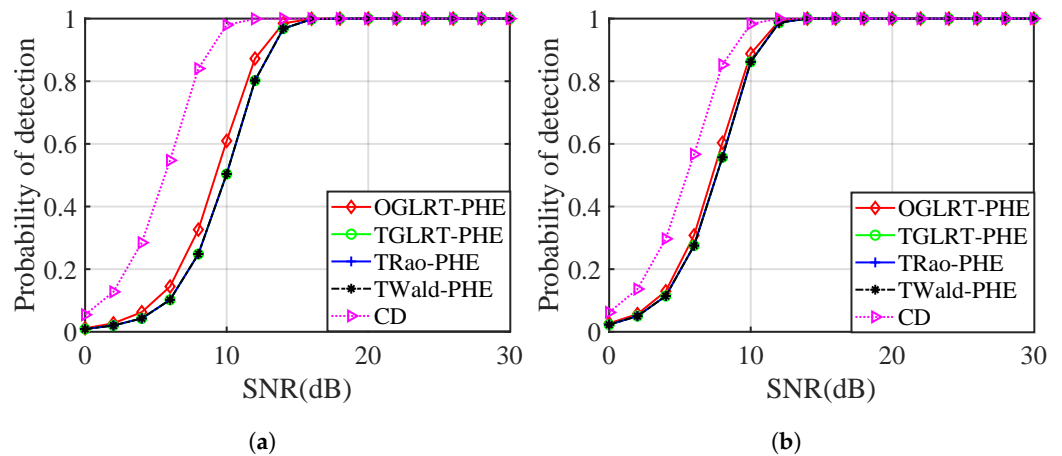
Figure 2. PD versus SNR for different cases of *K*. (**a**) $K = 4$, (**b**) $K = 8$.
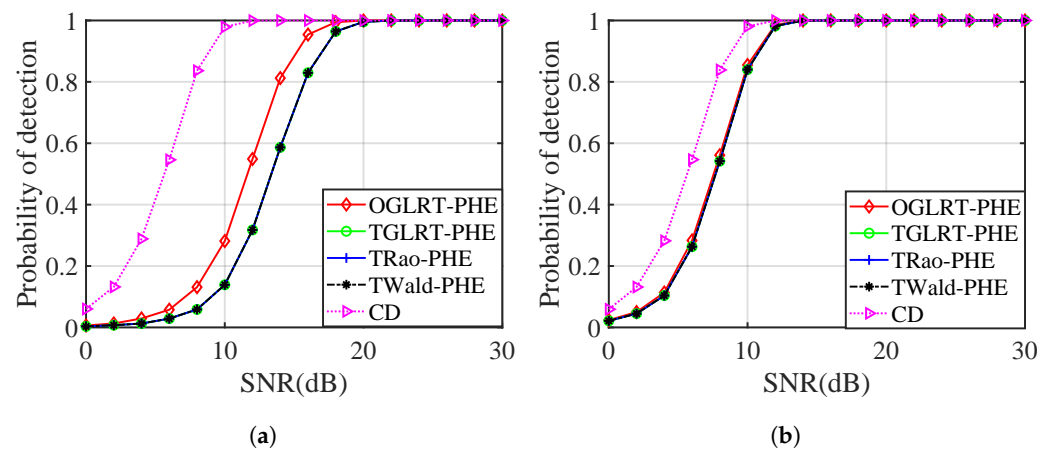
Figure 3. PD versus SNR for different cases of *L*. (**a**) $L = 4$, (**b**) $L = 12$.

Figure 4 demonstrates the detection performance of the proposed detectors where the frequency increment is set as $\Delta f = 10$ MHz. Together with Figure 2a, it can be found that the performance of all these detectors degrades significantly with the increase of the frequency increment Δf.
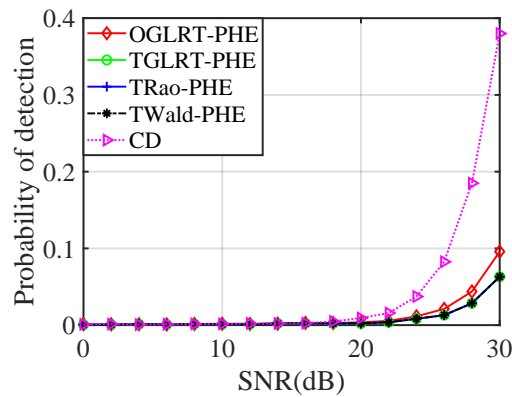
Figure 4. PD versus SNR with $\Delta f = 10$ MHz.

Figure 5 plots the detection performance of the proposed detectors against various power mismatch γ where SNR is set as $\xi_n = 0$ dB. The results indicate that the detection

performance of the proposed detector worsens as the power mismatch γ increases. The reason for this is that a larger power mismatch causes more disturbance, leading to poorer estimation precision of the covariance matrix **R**. Furthermore, the OGLRT-PHE detector still gains the highest PD among all the proposed detectors.
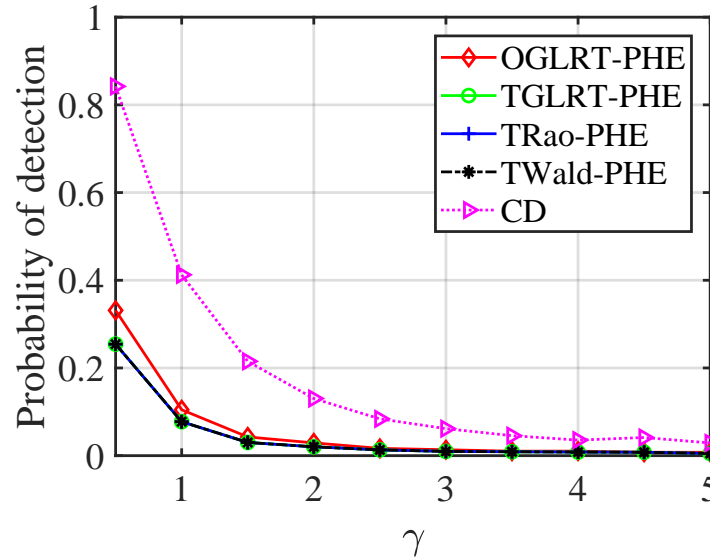
Figure 5. PD versus γ with $\xi_n = 0$ dB.

In practice, there can be inaccuracies in the array calibration and waveform matching, which can cause the actual steering vectors to deviate from the presumed ones. To measure the degree of these discrepancies, we employ two parameters—$\cos^2(\phi_1)$ and $\cos^2(\phi_2)$—which are defined as

$$\cos^2(\phi_1) = \frac{\left|\mathbf{a}_{tr}^H(r_s, \theta_s)\mathbf{R}^{-1}\mathbf{a}_{tr}(r_0, \theta_0)\right|}{\mathbf{a}_{tr}^H(r_s, \theta_s)\mathbf{R}^{-1}\mathbf{a}_{tr}(r_s, \theta_s)\mathbf{a}_{tr}^H(r_0, \theta_0)\mathbf{R}^{-1}\mathbf{a}_{tr}(r_0, \theta_0)}, \tag{75}$$

and

$$\cos^2(\phi_2) = \frac{\left|\mathbf{w}_d^H(f_{d,0})\mathbf{w}_d(f_{d,s})\right|^2}{\left\|\mathbf{w}_d^H(f_{d,0})\right\|^2 \left\|\mathbf{w}_d(f_{d,s})\right\|^2}, \tag{76}$$

respectively. Here, $\mathbf{a}_{tr}(r_0, \theta_0)$ and $\mathbf{w}_d(f_{d,0})$ representing the actual transmit-receive steering vector and the actual Doppler steering vector, respectively. Smaller values of $\cos^2(\phi_1)$ and $\cos^2(\phi_2)$ indicate a more severe mismatch.

Figure 6 depicts the detection performance of the proposed detectors in the presence of steering vector mismatches. The figure shows three scenarios: Figure 6a only the transmit-receive steering vector mismatch exists ($\cos^2(\phi_1) = 0.8$), Figure 6b only the Doppler steering vector mismatch exists ($\cos^2(\phi_2) = 0.8$), and Figure 6c both transmit-receive and Doppler steering vector mismatches exist ($\cos^2(\phi_1) = 0.8$ and $\cos^2(\phi_2) = 0.8$). When compared to Figure 2a, it is clear that all the proposed detectors' performances decline in the presence of steering vector mismatches, with the OGLRT-PHE detector having the fastest decline in PD. The effect of the Doppler steering vector mismatch on the PDs is more significant when there is a single steering vector mismatch. On the other hand, when both steering vector mismatches exist, the TGLRT-PHE, TRao-PHE, and TWald-PHE detectors have higher PDs, indicating that these three detectors are more robust.

(a)

(b)

(c)
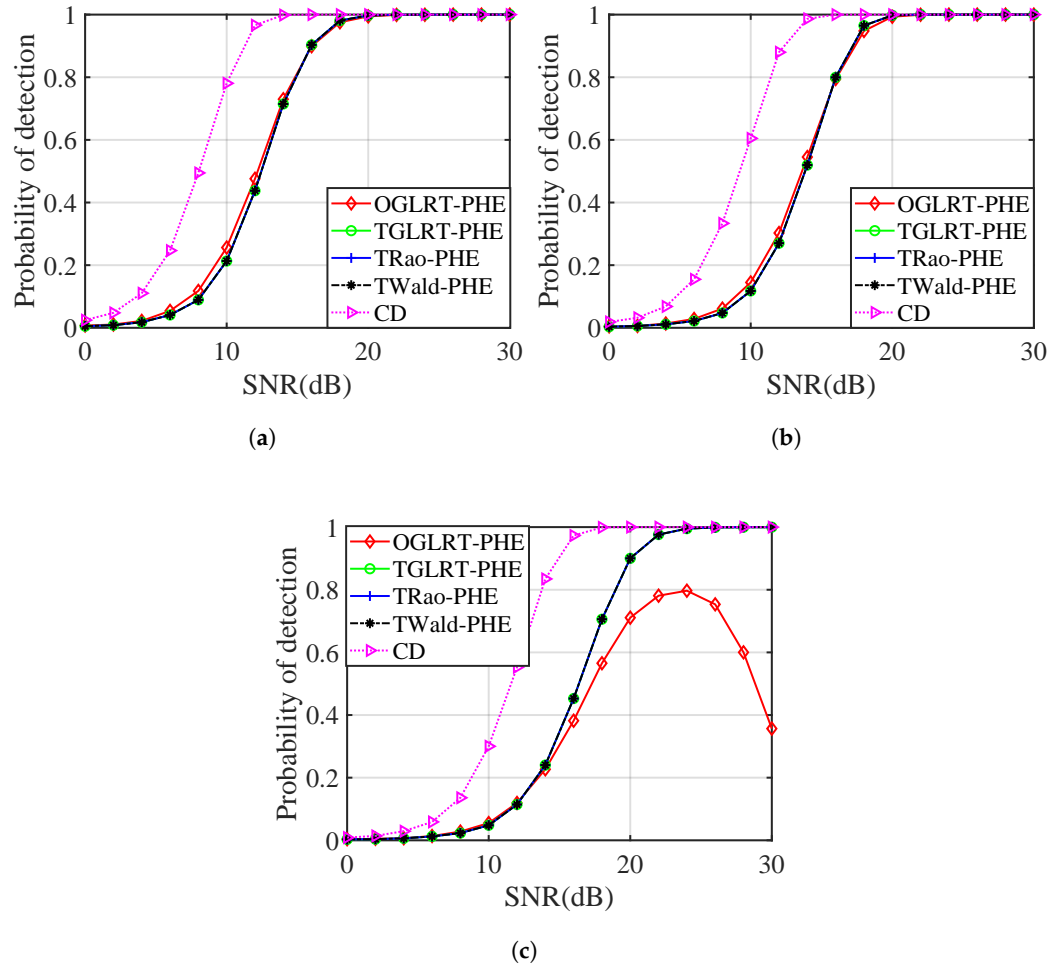
Figure 6. PD versus SNR for different cases of steering vector mismatch. (**a**) $\cos^2(\phi_1) = 0.8$, (**b**) $\cos^2(\phi_2) = 0.8$. (**c**) $\cos^2(\phi_1) = 0.8$ and $\cos^2(\phi_2) = 0.8$.

For comparison, we introduce detectors based on OGLRT, TGLRT, TRao, and TWald criteria in a homogeneous environment. Their statistical expressions are [28,41]:

$$\Lambda_{OGLRT-HE} = \frac{1 + \frac{\mathbf{w}_d^T \tilde{\mathbf{X}}^H \tilde{\mathbf{X}} \mathbf{w}_d^*}{\mathbf{w}_d^T \mathbf{w}_d^*}}{1 + \frac{\mathbf{w}_d^T \tilde{\mathbf{X}}^H \mathbf{P}_{\tilde{\mathbf{a}}}^{\perp} \tilde{\mathbf{X}} \mathbf{w}_d^*}{\mathbf{w}_d^T \mathbf{w}_d^*}}, \tag{77}$$

and

$$\Lambda_{TS-HE} = \mathrm{tr}\left(\mathbf{P}_{\mathbf{w}_d^*} \tilde{\mathbf{X}}^H \mathbf{P}_{\tilde{\mathbf{a}}} \tilde{\mathbf{X}} \mathbf{P}_{\mathbf{w}_d^*}\right) = \mathbf{w}_d^T \tilde{\mathbf{X}}^H \mathbf{P}_{\tilde{\mathbf{a}}} \tilde{\mathbf{X}} \mathbf{w}_d^*, \tag{78}$$

respectively, with $\mathbf{P}_{\tilde{\mathbf{a}}}$ and $\mathbf{P}_{\tilde{\mathbf{a}}}^{\perp}$ being defined in Appendix A. Here, the expressions for the TGLRT, TRao, and TWald detectors in homogeneous environments are all equivalently uniform to the TS-HE detector.

Figure 7 displays the detection performance of all detectors in homogeneous environments. Notably, the proposed detectors demonstrate comparable performance to those derived from homogeneous environments and even exhibit a slight advantage. This outcome serves as a validation of the effectiveness of the proposed detectors.
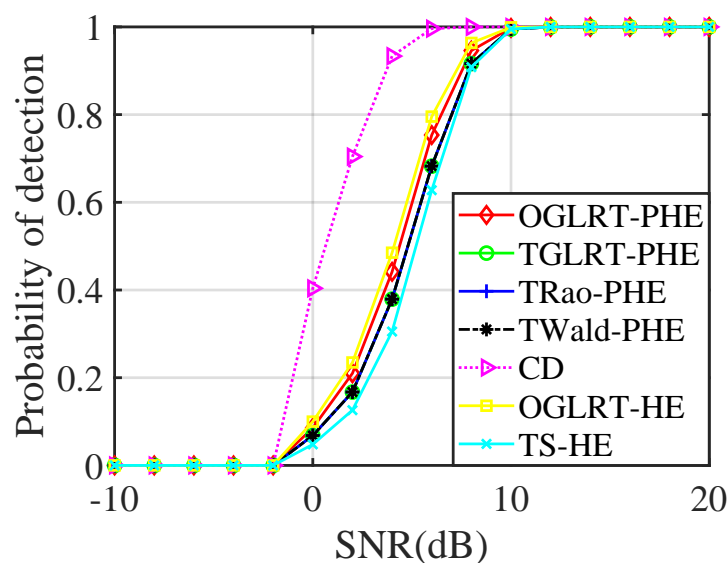
Figure 7. PD versus SNR in HE ($\gamma = 1$).

6. Conclusions

In this paper, we comprehensively explored the problem of adaptive moving-target detection in partially homogeneous environments for an FDA-MIMO radar platform. Based on different criteria, OGLRT-PHE, TGLRT-PHE, TRao-PHE, and TWald-PHE detectors with CFAR properties were derived using training data. Numerical experiments show that the OGLRT-PHE detector performs optimally, while the rest of the proposed detectors are more robust to signal mismatch. Moreover, these proposed detectors perform comparably to detectors designed for homogeneous environments, even in such environments. For future work, the detection problem for FDA-MIMO radar in compound Gaussian disturbance and other nonhomogeneous environments deserves further investigation. Moreover, Durbin and gradient tests can also provide new methods for FDA-MIMO radar target detection.

Author Contributions: Conceptualization, C.H. and B.H.; methodology, C.H., B.H. and Y.J.; validation, R.Z. and Z.W.; data analysis M.X. and L.L.; writing—original draft preparation, C.H., B.H. and M.X.; writing—review and editing, C.H., R.Z., Z.W., Z.L. and Y.J.; funding acquisition, Z.L. and Y.J. All authors have read and agreed to the published version of the manuscript.

Data Availability Statement: Data are contained within the article.

Conflicts of Interest: The authors declare no conflict of interest.

Abbreviations

The following abbreviations are used in this manuscript:

FDA	frequency diverse array
MIMO	multiple-input multiple-output
FDA-MIMO	frequency diverse array multiple-input multiple-output
PA	phased array
DOF	degree of freedom
GLRT	generalized maximum likelihood ratio test
UGLRT	unstructured generalized likelihood ratio test

OGLRT	one-step GLRT
TGLRT	two-step GLRT
TRao	two-step Rao
TWald	two-step Wald
HE	homogeneous environments
PHE	partially homogeneous environments
CFAR	constant false-alarm rate
HRWS-SAR	high-resolution and wide-swath synthetic aperture radar
ICM	interference covariance matrix
CUT	cell under test
RCS	radar cross section
IID	independent and identically distributed
PDF	probability density function
SCM	sample covariance matrix
MLE	maximum likelihood estimate
w.r.t	with respect to
NCM	noise covariance matrix
FIM	Fisher information matrix
PD	probability of detection
PFA	probability of false alarm
SNR	signal-to-noise ratio
JNR	jamming-to-noise ratio
MC	Monte Carlo

Appendix A. Deviation of (20) and (21)

Please note that $\tilde{\mathbf{X}}_{\alpha_s}^H \tilde{\mathbf{X}}_{\alpha_s}$ in (19) can be decomposed into

$$\tilde{\mathbf{X}}_{\alpha_s}^H \tilde{\mathbf{X}}_{\alpha_s} = \tilde{\mathbf{X}}_{\alpha_s}^{||H} \tilde{\mathbf{X}}_{\alpha_s}^{||} + \tilde{\mathbf{X}}^{\perp H} \tilde{\mathbf{X}}^{\perp}, \tag{A1}$$

where $\tilde{\mathbf{X}}_{\alpha_s}^{||} = \mathbf{P}_{\tilde{\mathbf{a}}} \tilde{\mathbf{X}}_{\alpha_s} = \mathbf{P}_{\tilde{\mathbf{a}}} \tilde{\mathbf{X}} - \alpha_s \tilde{\mathbf{a}} \mathbf{w}_d^T$ and $\tilde{\mathbf{X}}^{\perp} = \mathbf{P}_{\tilde{\mathbf{a}}}^{\perp} \tilde{\mathbf{X}}_{\alpha_s} = \mathbf{P}_{\tilde{\mathbf{a}}}^{\perp} \tilde{\mathbf{X}}$, with $\mathbf{P}_{\tilde{\mathbf{a}}} = \frac{\tilde{\mathbf{a}} \tilde{\mathbf{a}}^H}{\tilde{\mathbf{a}}^H \tilde{\mathbf{a}}}$ and $\mathbf{P}_{\tilde{\mathbf{a}}}^{\perp} = \mathbf{I}_{MN} - \mathbf{P}_{\tilde{\mathbf{a}}}$ being the projection matrix and the orthogonal projection matrix onto the column space of $\tilde{\mathbf{a}}$, respectively. Using the inequality $\det(\mathbf{A} + \mathbf{B}) \geq \det(\mathbf{A})$ [43], where $\mathbf{A} \in \mathbb{C}^{M \times M}$ is positive define matrix and $\mathbf{B} \in \mathbb{C}^{M \times M}$ is positive semi-define matrix, we have,

$$
\begin{aligned}
\min_{\alpha_s \in \mathbb{C}} f(\alpha_s) &= \min_{\alpha_s \in \mathbb{C}} \det\left[\mathbf{I}_K + \frac{\tilde{\mathbf{X}}_{\alpha_s}^{||H} \tilde{\mathbf{X}}_{\alpha_s}^{||} + \tilde{\mathbf{X}}^{\perp H} \tilde{\mathbf{X}}^{\perp}}{\gamma} \right] \\
&= \min_{\alpha_s \in \mathbb{C}} \det\left[\left(\mathbf{I}_K + \frac{\tilde{\mathbf{X}}^{\perp H} \tilde{\mathbf{X}}^{\perp}}{\gamma} \right) + \frac{\tilde{\mathbf{X}}_{\alpha_s}^{||H} \tilde{\mathbf{X}}_{\alpha_s}^{||}}{\gamma} \right] \\
&= \det\left(\mathbf{I}_K + \frac{\tilde{\mathbf{X}}^{\perp H} \tilde{\mathbf{X}}^{\perp}}{\gamma} \right).
\end{aligned}
\tag{A2}
$$

When the minimum is obtained, $\tilde{\mathbf{X}}_{\alpha_s}^{||H} \tilde{\mathbf{X}}_{\alpha_s}^{||} = \mathbf{0}_{K \times K}$, i.e., $\tilde{\mathbf{X}}_{\alpha_s}^{||} = \mathbf{0}_{MN \times K}$, that leads to

$$\alpha_s \tilde{\mathbf{a}} \mathbf{w}_d^T = \mathbf{P}_{\tilde{\mathbf{a}}} \tilde{\mathbf{X}}. \tag{A3}$$

Pre-multiplying both sides of (A3) by $\tilde{\mathbf{a}}^H$ yields

$$\alpha_s \tilde{\mathbf{a}}^H \tilde{\mathbf{a}} \mathbf{w}_d^T = \tilde{\mathbf{a}}^H \mathbf{P}_{\tilde{\mathbf{a}}} \tilde{\mathbf{X}}. \tag{A4}$$

Post-multiplying both sides of (A4) by $\mathbf{w}_d^*$, after sorting, it leads to

$$\hat{\alpha}_s = \frac{\tilde{\mathbf{a}}^H \mathbf{P}_{\tilde{\mathbf{a}}} \tilde{\mathbf{X}}}{\tilde{\mathbf{a}}^H \tilde{\mathbf{a}}} \mathbf{w}_d^* = \frac{\tilde{\mathbf{a}}^H \tilde{\mathbf{X}} \mathbf{w}_d^*}{\tilde{\mathbf{a}}^H \tilde{\mathbf{a}}}, \tag{A5}$$

where the fact $\mathbf{w}_d^T \mathbf{w}_d^* = 1$ is used again.

Obviously, the minimum at this point can be rewritten as

$$
\begin{aligned}
\min_{\alpha_s \in \mathbb{C}} f(\alpha_s) = f(\hat{\alpha}_s) &= \det\left(\mathbf{I}_K + \frac{\tilde{\mathbf{X}}^{\perp H} \tilde{\mathbf{X}}^{\perp}}{\gamma} \right) \\
&= \det\left(\mathbf{I}_K + \frac{\tilde{\mathbf{X}}_{\hat{\alpha}_s}^H \tilde{\mathbf{X}}_{\hat{\alpha}_s}}{\gamma} \right) \\
&= \det\left(\mathbf{I}_K + \frac{\left(\tilde{\mathbf{X}} - \hat{\alpha}_s \tilde{\mathbf{a}} \mathbf{w}_d^T\right)^H \left(\tilde{\mathbf{X}} - \hat{\alpha}_s \tilde{\mathbf{a}} \mathbf{w}_d^T\right)}{\gamma} \right) \\
&= \det\left[\mathbf{I}_K + \frac{\left(\tilde{\mathbf{X}} - \mathbf{P}_{\tilde{\mathbf{a}}} \tilde{\mathbf{X}} \mathbf{w}_d^* \mathbf{w}_d^T\right)^H \left(\tilde{\mathbf{X}} - \mathbf{P}_{\tilde{\mathbf{a}}} \tilde{\mathbf{X}} \mathbf{w}_d^* \mathbf{w}_d^T\right)}{\gamma} \right],
\end{aligned}
\tag{A6}
$$

with $\tilde{\mathbf{X}}_{\hat{\alpha}_s} = \tilde{\mathbf{X}} - \hat{\alpha}_s \tilde{\mathbf{a}} \mathbf{w}_d^T$. Or, in another way, directly plugging (A5) into (19) also can attain the minimum.

Appendix B. Deviation of (26)

The numerator and denominator of (25) share the same expression form as

$$
f(\gamma) = \gamma^{\frac{MN}{L+1}} \det\left[\mathbf{I}_{MN} + \frac{\mathbf{A}}{\gamma} \right] = \gamma^{\frac{MN}{L+1}} \prod_{r=1}^{R} \left(1 + \frac{\delta_r}{\gamma} \right),
\tag{A7}
$$

where $\mathbf{A} \in \mathbb{C}^{K \times K}$ is positive semi-define matrix with rank R and non-zero eigenvalues $\delta_r (r = 1, \cdots, R)$. Taking the derivative of (A7) regarding γ, we have

$$
\begin{aligned}
\frac{df(\gamma)}{d\gamma} &= \frac{MN}{L+1} \gamma^{\frac{MN}{L+1}-1} \left[\frac{MN}{L+1} \prod_{r=1}^{R} \left(1 + \frac{\delta_r}{\gamma} \right) - \sum_{i=1}^{R} \frac{\delta_i}{\gamma} \prod_{j=1, j \neq i}^{R} \left(1 + \frac{\delta_j}{\gamma} \right) \right] \\
&= \gamma^{\frac{MN}{L+1}-1} \prod_{r=1}^{R} \left(1 + \frac{\delta_r}{\gamma} \right) \left(\frac{MN}{L+1} - \sum_{r=1}^{R} \frac{\delta_r}{\gamma + \delta_r} \right).
\end{aligned}
\tag{A8}
$$

Define

$$
g(\gamma) = \sum_{r=1}^{R} \frac{\delta_r}{\gamma + \delta_r}.
\tag{A9}
$$

Clearly, $g(\gamma)$ is continuous and monotonically decreasing over $\gamma \in (0, +\infty)$, thus we have

$$
\max_{\gamma} g(\gamma) = g(0) = R,
\tag{A10}
$$

and

$$
\min_{\gamma} g(\gamma) = g(+\infty) = 0.
\tag{A11}
$$

Therefore, if $\frac{MN}{L+1} \in (0, R)$, there is a unique positive value of γ satisfying $\frac{df(\gamma)}{d\gamma} = 0$ by solving the equation $\frac{MN}{L+1} = \sum_{i=1}^{R} \frac{\delta_i}{\gamma + \delta_i}$. Otherwise, namely $\frac{MN}{L+1} \geq R$, it follows that $\frac{df(\gamma)}{d\gamma} \geq 0$, $\forall \gamma \in (0, +\infty)$, hence, the minimum of $f(\gamma)$ occurs at $\gamma = 0$. The latter case should be excluded because γ corresponding to the minimum of $f(\gamma)$ is out of the range. In summary, $f(\gamma)$ attains its minimum regarding $\gamma \in (0, +\infty)$ as the solution of $\frac{MN}{L+1} = \sum_{i=1}^{R} \frac{\delta_i}{\gamma + \delta_i}$.

Now, we go back to (25). For the numerator, there is $\mathbf{A} = \tilde{\mathbf{X}}^H \tilde{\mathbf{X}}$ and its non-zero eigenvalues $\delta_{r,0}$s, $(r = 1, \cdots, R)$. For the denominator, there is $\mathbf{A} = \left(\tilde{\mathbf{X}} - \mathbf{P}_{\tilde{\mathbf{a}}} \tilde{\mathbf{X}} \mathbf{w}_d^* \mathbf{w}_d^T \right) \times$

$\left(\tilde{\mathbf{X}} - \mathbf{P}_{\tilde{\mathbf{a}}}\tilde{\mathbf{X}}\mathbf{w}_d^* \mathbf{w}_d^T\right)^H$ and its non-zero eigenvalues $\delta_{r,1}$s, $(r = 1, \cdots, R)$. Herein, $R = \min (MN, K)$.

References

1. Antonik, P.; Wicks, M.; Griffiths, H.; Baker, C. Frequency diverse array radars. In Proceedings of the 2006 IEEE Conference on Radar, Verona, NY, USA, 24–27 April 2006; p. 3. [CrossRef]
2. Gao, K.; Wang, W.Q.; Cai, J.; Xiong, J. Decoupled frequency diverse array range- angle-dependent beampattern synthesis using non-linearly increasing frequency offsets. *IET Microwaves Antennas Propag.* **2016**, *10*, 880–884. [CrossRef]
3. Xu, J.; Liao, G.; Zhang, Y.; Ji, H.; Huang, L. An Adaptive Range-Angle-Doppler Processing Approach for FDA-MIMO Radar Using Three-Dimensional Localization. *IEEE J. Sel. Top. Signal Process.* **2017**, *11*, 309–320. [CrossRef]
4. Basit, A.; Wang, W.Q.; Nusenu, S.Y.; Wali, S. FDA Based QSM for mmWave Wireless Communications: Frequency Diverse Transmitter and Reduced Complexity Receiver. *IEEE Trans. Wirel. Commun.* **2021**, *20*, 4571–4584. [CrossRef]
5. Gui, R.; Huang, B.; Wang, W.Q.; Sun, Y. Generalized Ambiguity Function for FDA Radar Joint Range, Angle and Doppler Resolution Evaluation. *IEEE Geosci. Remote Sens. Lett.* **2020**, *19*, 3502305. [CrossRef]
6. Bang, H.; Yan, Y.; Basit, A.; Wang, W.Q.; Cheng, J. Radar Cross Section Characterization of Frequency Diverse Array Radar. *IEEE Trans. Aerosp. Electron. Syst.* **2023**, *59*, 460–471. [CrossRef]
7. Li, J.; Stoica, P. *MIMO Radar Signal Processing*; John Wiley & Sons, Inc.: Hoboken, NJ, USA, 2008.
8. Tan, M.; Wang, C.; Li, Z. Correction Analysis of Frequency Diverse Array Radar About Time. *IEEE Trans. Antennas Propag.* **2021**, *69*, 834–847. [CrossRef]
9. Lan, L.; Xu, J.; Liao, G.; Zhang, Y.; So, H.C. Suppression of Mainbeam Deceptive Jammer with FDA-MIMO Radar. *IEEE Trans. Veh. Technol.* **2020**, *69*, 11584–11598. [CrossRef]
10. Xu, J.; Liao, G.; Zhu, S.; Huang, L.; So, H.C. Joint Range and Angle Estimation Using MIMO Radar with Frequency Diverse Array. *IEEE Trans. Signal Process.* **2015**, *63*, 3396–3410. [CrossRef]
11. Ji, S.; Wang, W.Q.; Chen, H.; Zhang, S. On Physical-Layer Security of FDA Communications Over Rayleigh Fading Channels. *IEEE Trans. Cogn. Commun. Netw.* **2019**, *5*, 476–490. [CrossRef]
12. Zhou, Y.; Wang, W.; Chen, Z.; Zhao, Q.; Deng, Y.; Wang, R. A Novel High-Resolution and Wide-Swath SAR Imaging Mode Using Frequency Diverse Planar Array. In Proceedings of the EUSAR 2021, 13th European Conference on Synthetic Aperture Radar, Virtal Event, 29 March–1 April 2021; pp. 1–5.
13. Zhou, Y.; Wang, W.; Chen, Z.; Zhao, Q.; Zhang, H.; Deng, Y.; Wang, R. High-Resolution and Wide-Swath SAR Imaging Mode Using Frequency Diverse Planar Array. *IEEE Geosci. Remote Sens. Lett.* **2021**, *18*, 321–325. [CrossRef]
14. Huang, B.; Wang, W.Q.; Zhang, S.; Wang, H.; Gui, R.; Lu, Z. A Novel Approach for Spaceborne SAR Scattered-Wave Deception Jamming Using Frequency Diverse Array. *IEEE Geosci. Remote Sens. Lett.* **2020**, *17*, 1568–1572. [CrossRef]
15. Bang, H.; Wang, W.Q.; Zhang, S.; Liao, Y. FDA-Based Space–Time–Frequency Deceptive Jamming Against SAR Imaging. *IEEE Trans. Aerosp. Electron. Syst.* **2022**, *58*, 2127–2140. [CrossRef]
16. Huang, L.; Zong, Z.; Zhang, S.; Wang, W.Q. 2-D Moving Target Deception Against Multichannel SAR-GMTI Using Frequency Diverse Array. *IEEE Geosci. Remote Sens. Lett.* **2022**, *19*, 4006705. [CrossRef]
17. Cheng, J.; Wang, W.Q.; Zhang, S. Joint MIMO and Frequency Diverse Array for Suppressing Mainlobe Interferences. In Proceedings of the International Symposium on Antennas and Propagation, Osaka, Japan, 25–28 January 2021.
18. Gui, R.; Wang, W.Q.; Farina, A.; So, H.C. FDA radar with doppler-spreading consideration: Mainlobe clutter suppression for blind-doppler target detection. *Signal Process.* **2021**, *179*, 107773. [CrossRef]
19. Lan, L.; Liao, G.; Xu, J.; Zhang, Y.; Fioranelli, F. Suppression Approach to Main-Beam Deceptive Jamming in FDA-MIMO Radar Using Nonhomogeneous Sample Detection. *IEEE Access* **2018**, *6*, 34582–34597. [CrossRef]
20. Zhang, Y.; Liao, G.; Xu, J.; Lan, L. Mainlobe Deceptive Jammer Suppression Based on Quadratic Phase Coding in FDA-MIMO Radar. *Remote Sens.* **2022**, *14*, 5831. [CrossRef]
21. Wan, P.; Weng, Y.; Xu, J.; Liao, G. Range Gate Pull-Off Mainlobe Jamming Suppression Approach with FDA-MIMO Radar: Theoretical Formalism and Numerical Study. *Remote Sens.* **2022**, *14*, 1499. [CrossRef]
22. Lan, L.; Marino, A.; Aubry, A.; Maio, A.D.; Zhang, Y. GLRT-based Adaptive Target Detection in FDA-MIMO Radar. *IEEE Trans. Aerosp. Electron. Syst.* **2020**, *57*, 597–613. [CrossRef]
23. Gui, R.; Wang, W.Q.; Zheng, Z. Low-complexity GLRT for FDA radar without training data. *Digit. Signal Process.* **2020**, *107*, 102861. [CrossRef]
24. Zhu, Y.; Liu, L.; Lu, Z.; Zhang, S. Target Detection Performance Analysis of FDA-MIMO Radar. *IEEE Access* **2019**, *7*, 164276–164285. [CrossRef]
25. Huang, B.; Basit, A.; Gui, R.; Wang, W.Q. Adaptive Moving Target Detection Without Training Data for FDA-MIMO Radar. *IEEE Trans. Veh. Technol.* **2022**, *71*, 220–232. [CrossRef]
26. Xu, J.; Zhu, S.; Liao, G. Range Ambiguous Clutter Suppression for Airborne FDA-STAP Radar. *IEEE J. Sel. Top. Signal Process.* **2015**, *9*, 1620–1631. [CrossRef]

27. Chen, X.; Chen, B.; Guan, J.; Huang, Y.; He, Y. Space-Range-Doppler Focus-Based Low-observable Moving Target Detection Using Frequency Diverse Array MIMO Radar. *IEEE Access* **2018**, *6*, 43892–43904. [CrossRef]
28. Zeng, L.; Wang, Y.L.; Liu, W.; Liu, J.; Lan, L. GLRT-based detectors for FDA-MIMO radar with training data. *Digit. Signal Process.* **2022**, *130*, 103729. [CrossRef]
29. Kraut, S.; Scharf, L.L. The CFAR Adaptive Subspace Detector is a Scale-Invariant GLRT. *IEEE Trans. Signal Process.* **1999**, *47*, 2538. [CrossRef]
30. Liu, W.; Xie, W.; Liu, J.; Wang, Y. Adaptive Double Subspace Signal Detection in Gaussian Background—Part II: Partially Homogeneous Environments. *IEEE Trans. Signal Process.* **2014**, *62*, 2358–2369. [CrossRef]
31. Dong, Y.; Ming, L.; Kai, L.; Tang, Z.; Liu, W. Adaptive Direction Detection in Deterministic Interference and Partially Homogeneous Noise. *IEEE Signal Process. Lett.* **2017**, *24*, 599–603. [CrossRef]
32. Liu, J.; Liu, W.; Hao, C.; Orlando, D.; Farina, A. Robust GLRT Detection Exploiting Persymmetry in Partially Homogeneous Environments. In Proceedings of the 2019 International Conference on Control, Automation and Information Sciences (ICCAIS), Chengdu, China, 23–26 October 2019; pp. 1–6. [CrossRef]
33. Huang, C.; Wang, Y.; Liu, W.; Liu, J.; Du, Q. Adaptive Detection with Training Data in Partially Homogeneous Environments for Colocated MIMO Radar. *Signal Process.* **2023**, *217*, 109353. [CrossRef]
34. Pulsone, N.; Rader, C. Adaptive beamformer orthogonal rejection test. *IEEE Trans. Signal Process.* **2001**, *49*, 521–529. [CrossRef]
35. Bandiera, F.; Orlando, D.; Ricci, G. *Advanced Radar Detection Schemes Under Mismatched Signal Models*; Synthesis Lectures on Signal Processing Series; Springer: Cham, Switzerland, 2009; Volume 4, pp. 1–105. [CrossRef]
36. Gui, R.; Wang, W.Q.; Shao, H. General receiver design for FDA radar. In Proceedings of the 2018 IEEE Radar Conference (RadarConf18),Oklahoma City, OK, USA, 23–27 April 2018.
37. Kelly, E. An Adaptive Detection Algorithm. *IEEE Trans. Aerosp. Electron. Syst.* **1986**, *AES-22*, 115–127. [CrossRef]
38. Kelly, E.J.; Forsythe, K.M. *Adaptive Detection and Parameter Estimation for Multidimensional Signal Models*; NASA STI/Recon Technical Report N; MIT Lincoln Laboratory: Lexington, MA, USA, 1989.
39. Conte, E.; Maio, A.D.; Ricci, G. GLRT-based adaptive detection algorithms for range-spread targets. *IEEE Trans. Signal Process.* **2002**, *49*, 1336–1348. [CrossRef]
40. Liu, W.; Wang, Y.; Xie, W. Fisher information matrix, Rao test, and Wald test for complex-valued signals and their applications. *Signal Process.* **2014**, *94*, 1–5. [CrossRef]
41. Liu, W.; Xie, W.; Liu, J.; Wang, Y. Adaptive Double Subspace Signal Detection in Gaussian Background—Part I: Homogeneous Environments. *IEEE Trans. Signal Process.* **2014**, *62*, 2345–2357. [CrossRef]
42. Tague, J.A.; Caldwell, C.I. Expectations of useful complex Wishart forms. *Multidimens. Syst. Signal Process.* **1994**, *5*, 263–279. [CrossRef]
43. Zhang, X. *Matrix Analysis and Applications*; Cambridge University Press: Cambridge, UK, 2007; Volume 309, Part I, pp. 3–94.